Gait-level analysis of mouse open field behavior using deep learning-based pose estimation

Keith Sheppard[1], Justin Gardin[1], Gautam Sabnis[1], Asaf Peer[1], Megan Darrell[1], Sean Deats[1], Brian Geuther[1], Cathleen M. Lutz[1], and Vivek Kumar[1]

[1]The Jackson Laboratory

October 24, 2020

1 Abstract

Gait and whole body posture are sensitive measures of the proper functioning of numerous neural circuits, and are often perturbed in many neurological, neuromuscular, and neuropsychiatric illnesses. Rodents provide a tractable model for elucidating disease mechanisms and interventions, however, studying gait and whole body posture in rodent models requires specialized methods and remains challenging. Here, we develop a simple assay that allows adoption of the commonly used open field apparatus for gait and whole body posture analysis. We leverage modern neural networks to abstract a mouse into keypoints and extract gait and whole body coordination metrics of the animal. Gait-level analysis allows us to detect every step of the animal's movement and provides high resolution information about the animal's behavior. We quantitate gait and whole body posture with high precision and accuracy across 62 highly visually diverse strains of mice. We validate our approach using four genetic mutants with known gait deficits. In extended analysis, we demonstrate that multiple autism spectrum disorder (ASD) models show gait and posture deficits, implying this is a general feature of ASD. We conduct a large strain survey of over 1898 mice, and find that gait and whole body posture measures are highly heritable in the laboratory mouse, and fall into three classes. Furthermore, the reference mouse strain, C57BL/6J, has a distinctly different gait and posture compared to other standard laboratory and wild-derived strains. We conduct a genome wide association study (GWAS) to define the genetic architecture of mouse movement in the open field. Combined, we describe a simple, sensitive, accurate, scalable, and ethologically relevant method of mouse gait and whole body posture analysis for behavioral neurogenetics. These results provide one of the largest laboratory mouse gait-level data resources for the research community and show the utility of automated machine learning approaches for biological insights.

2 Introduction

In humans, the ability to quantitate gait and posture at high precision and sensitivity has shown that they can be used to determine proper function of numerous neural and muscular systems [1, 2]. Many psychiatric, neurodegenerative, and neuromuscular illnesses are associated with alterations in gait and posture, including autism spectrum disorder, schizophrenia, bipolar disorder, and Alzheimer's disease. [3–12]. This is because proper gait, balance, and posture are under the control of multiple nervous system processes [13, 14], which include critical sensory centers that process visual, vestibular, auditory, proprioceptive, and visceral inputs. Regions of the brain that directly control movement, such as the cerebellum, motor cortex, and brain stem, respond to cognitive and emotionality cues. Thus, gait and posture integrity reflects proper neural functioning of many neural systems in humans [13, 14]. In rodent models of human psychiatric conditions, to date there has not been conclusive demonstrated utility of gait and posture metrics as in humans. This is not necessarily because the models fail to faithfully recapitulate human phenotypes, but rather that we have lacked readily-implementable technology with sufficient accuracy to detect gait and posture differences between different mouse strains. The end result of this technological limitation is two-fold: rodent gait analysis remains tedious and often carried out only in expert labs with highly specialized equipment; and the behavioral neurogenetics field broadly has not been able to fully leverage relevant mouse gait phenotypes to understand the human disease. More importantly, while gait and movement analysis in humans is already a sensitive measure of numerous psychiatric illnesses, gait analysis in mice is generally used to study overt strong phenotypes. Thus, the ability to measure gait and whole body posture in an accurate, sensitive, and scalable manner is expected to enhance the utility of existing models and also lead to the development of better models of psychiatric endophenotypes.

Analysis of human and animal movement, including gait, has a storied past [15]. Aristotle was the first to write a philosophical treatise on animal movement and gait using physical and metaphysical principles [16]. During the Renaissance, Borelli applied the laws of physics and biomechanics to muscles, tendons, and joints of the entire body to understand gait [17]. The first application of imaging technologies to the study of gait is credited to the work of Muybridge and Marey, who took sequential photographic images of humans and animals in motion in order to derive quantitative measurements of gait [18–20]. Modern animal gait analysis methods are credited to Hildebrandt, who in the 1970s classified gait based on quantified metrics [21]. He defined a gait cycle in terms of contact of limb to the ground (stance and swing phases). Fundamentally, this concept has not changed over the past 40 years: while current methods of mouse gait analysis have increased efficiency of the imaging approaches of Muybridge and Marey, they are fundamentally still based on the timing of limbs contacting the ground. This is in contrast to human gait and posture analysis, which, since the time of Borelli, has focused on body posture, and is akin to the quantitation of whole body movement rather than just contact with the ground [22]. This difference between mouse and human is probably due in part to the difficulty in automatically estimating the posture of rodents, which appear as deformable objects due to their fur which obscures joint positions. In addition, unlike humans, parts of mice cannot be easily marked with wearables for localization. In rodents, recent methods have made progress in determination of whole body coordination, however, these still require specialized equipment and force the animal to walk in a fixed direction in a corridor or treadmill or a narrow corridor for proper imaging and accurate determination of limb position [23]. This is highly unnatural, and animals often require training to perform this behavior properly [24–27], limiting the use of this type of assay in correlating to human gait. Imaging from the side leads to perspective hurdles, which are overcome by limiting the movement of the animal to one depth field. Furthermore, as the animal defecates and urinates, or when bedding is present, the resulting occlusion makes long term monitoring from this perspective impractical. Indeed, ethologically relevant gait data in which animals can move freely often produce results that differ from treadmill-based assays [28]. Furthermore, commercial treadmill- or corridor-based systems for gait analysis often produce a plethora of measures that show differing results with same animal models [23, 29]. The exact causes of these disparities are challenging to determine with closed, proprietary systems. Thus, we currently lack a relatively easily

and broadly implementable tool to measure gait in free-moving animals.

The open field assay is one of the oldest and most commonly used assays in behavioral neurogenetics [30, 31]. In rodents, it has classically been used to measure endophenotypes associated with emotionality, such as hyperactivity, anxiety, exploration, and habituation in rodents [32]. For video based open field assays, rich and complex behaviors of animal movement are abstracted to a simple point in order to extract behavioral measures [33]. This oversimplified abstraction is necessary mainly due to technological limitations that have prohibited accurate extraction of complex poses from video data [34]. New technology has the potential to overcome this limitation [35, 36]. Gait, an important indicator of neural function, is not typically analyzed in the open field mainly due to the technical difficulty of determining limb position when animals are moving freely [23]. The ability to combine open field measures with gait and posture analysis would offer key insights into neural and genetic regulation of animal behavior in an ethologically relevant manner. Here, we leverage modern neural network methods to carry out mouse gait and posture analysis in the open field. We develop and apply a system to measure gait and whole body posture parameters from a top-down perspective that is invariant to the high level of visual diversity seen in the mouse, including coat color, fur differences, and size differences [37]. Altogether, we provide a methodology that is simple, sensitive, accurate, and scalable and can detect previously undescribed differences in gait and posture in mouse models of psychiatric illnesses. This method is a community resource for mouse movement in the open field that should commoditize gait analysis for behavioral neurogenetics.

3 Results

Our approach to gait and posture analysis is composed of several modular components. At the base of our toolkit is a deep convolutional neural network that has been trained to perform pose estimation on top-down video of an open field. This network provides twelve two-dimensional markers of mouse anatomical location, or "keypoints", for each frame of video describing the pose of the mouse at each time point. We have also developed downstream components that are capable of processing the time series of poses and identifying intervals that represent individual strides. These strides form the basis of almost all of the phenotypic and statistical analyses that follow. We can extract several important gait metrics on a per-stride basis because we have pose information for each stride interval (see Table 1 for a list of metrics). This gives us significant power to perform statistical analysis on stride metrics as well as allowing us to aggregate large amounts of data in order to provide consensus views of the structure of mouse gait.

3.1 Pose Estimation

Pose estimation locates the 2D coordinates of a pre-defined set of keypoints in an image or video, and is the foundation of our method for quantifying and analyzing gait. The selected pose keypoints are either visually salient, such as ears or nose, or capture important information for understanding pose, such as limb joints or paws. We thus selected twelve keypoints to capture mouse pose: nose, left ear, right ear, base of neck, left forepaw, right forepaw, mid spine, left hind paw, right hind paw, base of tail, mid tail and tip of tail (Figure 1 B).

Much effort has been spent developing and refining pose estimation techniques for human pose [38, 39]. Traditional approaches to pose estimation relied on techniques such as the use of local body part detectors and modeling of skeletal articulation. These approaches were limited in their ability to overcome complicating factors such as complex configurations and body part occlusion. The first major paper to address these shortcomings by developing a deep neural network for pose estimation was the DeepPose [40]. DeepPose was able to demonstrate improvements on the state-of-the-art performance for pose estimation using several

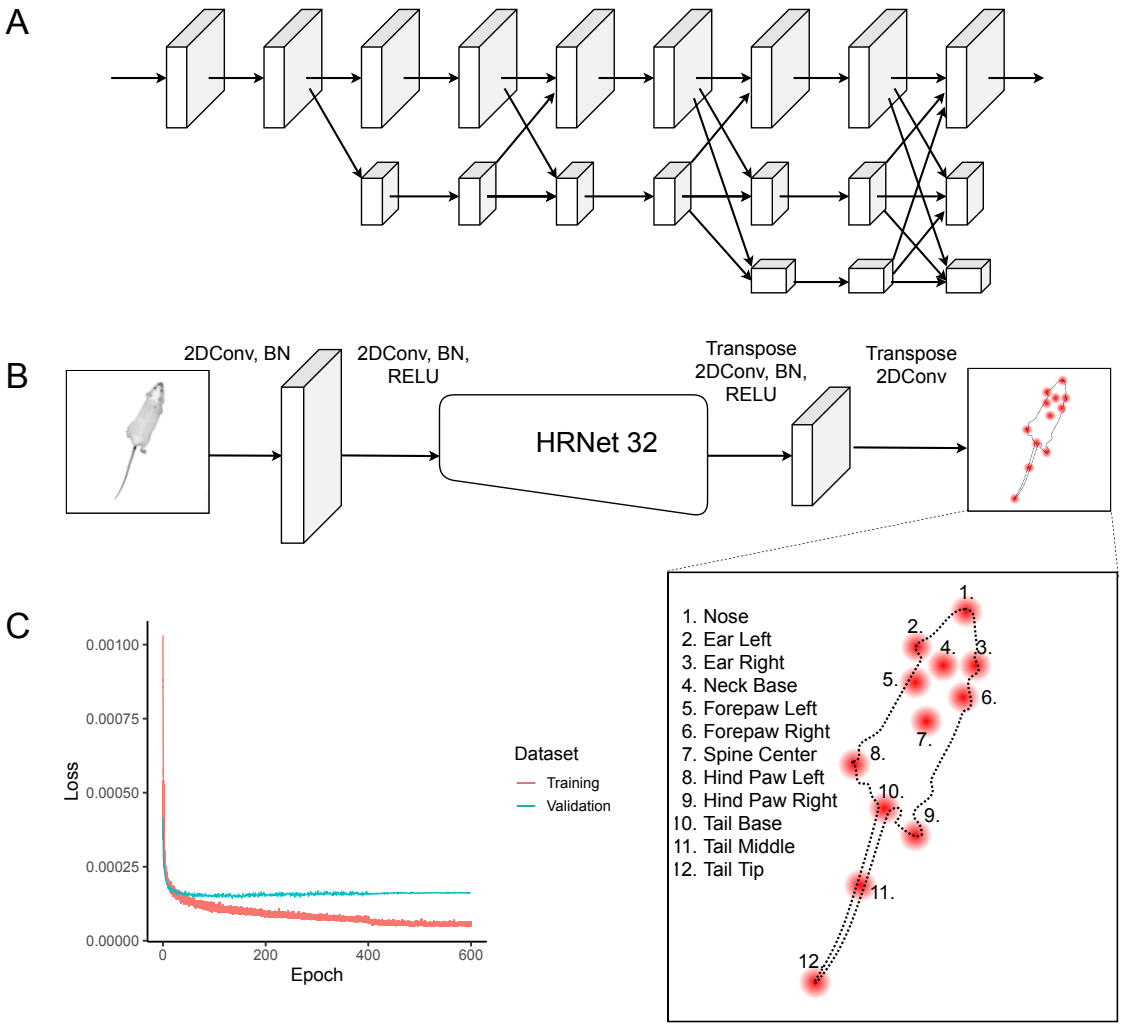

Figure 1: Deep convolutional neural network for pose estimation. (A) the HRNet-W32 neural network architecture for performing pose estimation. (B) The inference pipeline which sends video frames into the HRNet and generates twelve keypoint heatmaps as output. (C) Training loss curves show network convergence without overfitting.

benchmarks. After the publication of DeepPose, the majority of successful work on pose estimation leveraged deep convolutional neural network architectures. Some prominent examples include: DeeperCut [41], Stacked Hourglass Networks [42] and Deep High-Resolution architecture (HRNet) [43]. This is a rapidly evolving field and architectural improvements are frequently released and tracked by several leaderboards (https://paperswithcode.com/task/pose-estimation). Given this choice of high performance pose estimation architectures developed for human pose estimation, it made sense to leverage this prior work for our rodent pose estimation problem. There were several important considerations we based our pose estimation architecture selection upon.

- High accuracy and precision for pose inference: our gait inference method is sensitive to errors in pose estimation so we want to reduce those errors as much as possible
- Speed of inference: should be able to infer at or near real time speeds (30 fps) on a modern high end GPU
- Simplicity and generality of architecture to facilitate modification and extension.
- Fixed scale inference: because all of our images are at fixed scale, approaches that are designed to work at multiple scales waste network capacity and inference time.
- Available open source implementation
- Modularity of architecture in order to facilitate potential future upgrades.

Based on these criteria we selected the HRNet architecture [43] for our network and modified it for our experimental setup. The main differentiator of this architecture is that it maintains high resolution features throughout the network stack, thereby preserving spatial precision (Figure 1A). HRNet shows highly competitive performance in terms of both GPU efficiency and pose accuracy. The interface is also highly modular and is expected to allow for relatively simple network upgrades if needed. We used the smaller HRNet-W32 architecture rather than HRNet-W48 because it was shown to provide significant speed and memory improvements for only a small reduction in accuracy. We added two 5x5 transpose convolutions to the head of the network to match the heatmap output resolution with the resolution of the video input (Figure 1B). Because all of our experiments have a single mouse in an open field, we do not need to rely on object detection for instancing. We thus eliminated this step from our inference algorithm, which also leads to clear runtime performance benefits. Instead of performing pose estimation after object detection, we use the full resolution pose keypoint heatmaps to infer the posture of a single mouse at every frame. This means that for each 480x480 frame of video we generate 12 480x480 heatmaps (one heatmap per keypoint). The maximum value in each heatmap represents the highest confidence location for each respective point. Thus, after taking the argmax of each of the 12 heatmaps we have 12 (x, y) coordinates.

In order to train our network, we need to select a loss function and an optimization algorithm. For loss, we borrow the approach used in the original HRNet description [43]. For each keypoint label, we generate a 2D gaussian distribution centered on the respective keypoint. We then compare the output of the network with our keypoint-centered Gaussian and calculate loss as the mean squared difference between our labeled keypoint Gaussian and the heatmap generated by our network. We train our network using the ADAM optimization algorithm which is a variant of stochastic gradient descent [44]. Figure 1C shows that the validation loss converges rapidly. We intentionally generated labels that represent a wide diversity of mouse appearances, including variation in coat color, body length and obesity to ensure that the resulting network operates robustly across these differences. We hand labeled 8,910 frames across these diverse strains for training (see Methods). The resulting network is able to track dozens of mouse strains with varying body size, shape and coat color (Video S1) [37].

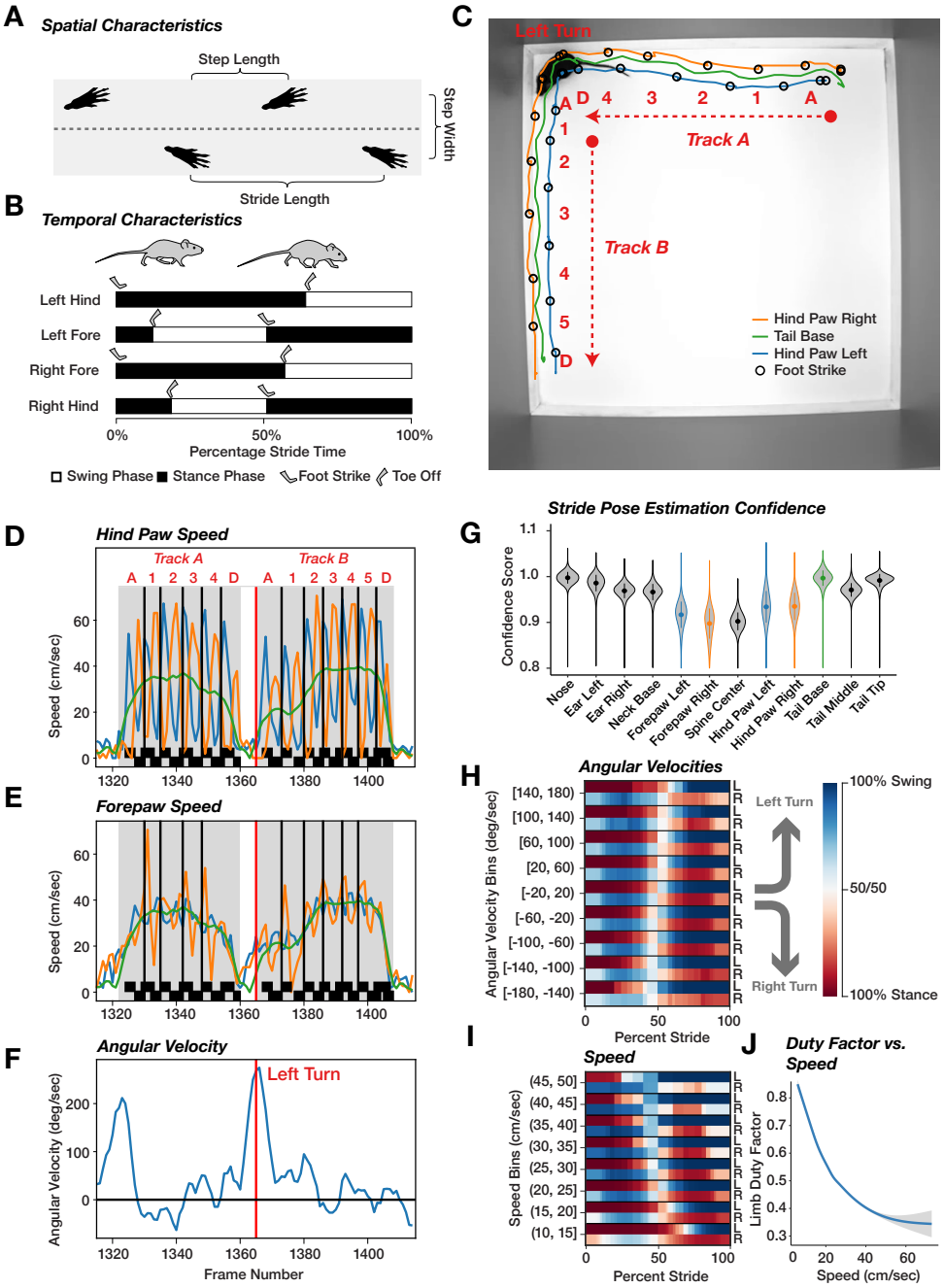

Figure 2: Extraction of gait metrics from video pose estimation. Spatial and temporal characteristics of gait (A, B, adapted from [23]). (A) An illustration showing how we derive three spatial stride metrics from hind paw foot strike positions: step length, step width and stride length. (B) All metrics shown in this Hildebrand plot have percent stride time for units. We see here the relationship between foot strike and toe off events with the stance and swing phases of stride. (C) A single frame of input video with hind paw tracks plotted fifty frames in the past and fifty frames in the future. The location of hind foot strike events is indicated with black circles and paths are shown (left hind paw (blue), right hind paw (orange), and base of tail (green)) for two sequences (track A and B). (D-F) Three plots showing different aspects of the mouse's movement over the same one hundred frame interval (Video S2). The centered red vertical line indicates the current frame (displayed in panel C). The top plot shows three lines indicating speed of the left hind paw (blue), the right hind paw (orange) and the base of tail (green). The vertical black lines in the plot indicate the inferred start frame of each stride. (G) The distribution of confidence values for each of the 12 keypoints we estimate. (H) Aggregate view of Hildebrand plot for hind paws binned according to angular velocity (left (L) and right (R)) shows changes in strike duration based on direction of turning. (I) Similar to panel (H) except binned by increasing speed and a fixed angular velocity (-20 to 20 deg/sec). (J) Limb duty factor changes as a function of speed.

3.2 Stride Inference

Our approach to detecting stride intervals is based on the cyclic structure of gait as described by Hildebrand (Figure 2A) [21, 45]. During a stride cycle, each of the paws has a stance phase and a swing phase [23]. During the stance phase, the mouse's paw is supporting the weight of the mouse and is in static contact with the ground. During the swing phase, the paw is moving forward and is not supporting the mouse's weight. Following Hildebrand, we refer to the transition from stance phase to swing phase as the toe-off event and the transition from swing phase to stance phase as the foot-strike event.

In order to calculate stride intervals, we determine stance and swing phases for the hind paws. We calculate paw speed and infer that a paw is in stance phase when the speed falls below a threshold and that it is in swing phase when it exceeds that threshold (Figure2C, D, E, F, Video S2). We can now determine that foot strike events occur at the transition frame from swing phase to stance phase (Figure2C). We define the left hind foot strike as the event that separates stride cycles. An example of the relationship between paw speed and foot strike events is shown in panel D of Figure 2 for hind paws. We find clean, high-amplitude oscillations of the hind paws, but not forepaws, as shown in panel E of Figure 2. This difference in inference quality between the forepaws and hind paws is likely due to the fact that forepaws are occluded more often than hind paws from the top-down view and are therefore more difficult to accurately locate. We observe a corresponding decrease in confidence of forepaw inferences as show in panel G of Figure 2. For this reason, we exclude forepaws from consideration when deriving stride intervals and focus instead on hind paws. We also perform a significant amount of filtering on strides to remove spurious or low quality stride cycles from our dataset (Figure2G). Criteria for removing strides include: low confidence or physiologically unrealistic pose estimates, missing right hind paw strike event, and insufficient overall body speed of mouse which is any speed under 10 cm/sec. Panel G of Figure 2 shows the distribution of confidences for each keypoint. Our filtering method uses 0.3 as a confidence threshold. Very high confidence keypoints are close to 1.0. We always remove the first and last strides in a continuous sequence of strides to avoid starting and stopping behaviors from adding noise to our stride data (Figure2C, D, labeled A and D, in Track A and B). This means that a sequence of seven strides will result in at most five strides being used for analysis. The distribution of keypoint confidence varies by keypoint type (Figure 2G). Keypoints which tend to be occluded in a top-down view such as fore paws have confidence distributions shifted down compared to other keypoints. We also see that keypoints that are not visually salient, such as the spine center, will have lower confidence since they are more difficult to locate precisely. Finally, we also calculate an instantaneous angular velocity which allows us to determine the directionality of each stride (Figure 2F). The angular velocity is calculated by taking the first derivative of the angle formed by the line that connects the base of the mouse's tail to the base of its neck. Combined, this approach allows us to identify individual high quality strides of a mouse in the open field.

In order to validate that our gait quantitation is functioning properly, we analyzed data from a commonly used inbred strain, C57BL/6NJ. We calculated percent of stance and swing from 15,667 strides from 31 animals using approximately 1-hour of open field video per mouse. We analyzed data from hind paws since these showed the highest amplitude oscillations during stance and swing (Figure 2D, E). We stratified the data into 9 angular velocity and 8 speed bins based on the tail base point (Figure 2H, I, respectively). As expected, we find increase in stance percent over a stride of the left hind paw when the animal is turning left. Reciprocally, when the animal is turning right, the stance percent of the right hind paw is increased (Figure 2H). We then analyzed strides in central angular velocity bin (-20 to 20 deg/sec) to determine if stance percent during a stride cycle decreases as the speed of the stride increases. We find the stance time decreases as the stride speed increases (Figure 2I). We calculated a duty factor for the hind paws to quantitate this relationship with speed (Figure 2J). Combined, we conclude that our methods are able to quantitatively and accurately extract strides from these open field videos from a top-down perspective.

After the stride intervals have been determined, we can use frame poses in conjunction with stance and

swing phase intervals to derive several stride metrics as defined in Table 1. We are able to extract all relevant spatiotemporal metrics from the hind paws, which serve as the primary data source for our statistical analyses [23].

3.3 Whole body posture estimation during gait cycle

Our top-down videos allow us to determine the relative position of the spine with 6 keypoints (nose, neck base, spine center, tail base, tail middle, and tail tip). With these, we extracted the whole body pose during a stride cycle, similar to previous work which carried this out with nose and tail pose only [46]. We used three points (nose, base of tail, and tip of tail) to capture the lateral movement during a stride cycle (Figure 3A, B, C, Video S3). These measures are circular, with opposite phases of the nose and the tip of tail. For display, we use C57BL/6J (Video S5, S6) and NOR/LtJ (Video S4, S6) which have different tip of tail phases during a stride cycle. We are able to extract these phase plots for each stride which provides high sensitivity (Figure 3 D, E, Video S3, S4, S5, S6). Since we have several hours of video across each strain, we are able to extract thousands of strides enabling high level of sensitivity. We can combine these at one speed and angular velocity bin to determine a consensus stride phase plot for each animal and strain (Figure 3F, G). Finally, we compared these phase plots between several strains and find striking diversity among whole body posture during the gait cycle.

Several of our metrics relate to the cyclic lateral displacement we observe in pose keypoints (Figure 3). Our measures of lateral displacement are defined as an orthogonal offset from the relevant stride displacement vector. We define the displacement vector as the line connecting the mouse's center of spine on the first frame of a stride to the mouse's center of spine on the last frame of stride. We calculate this offset at each frame of a stride and then perform a cubic interpolation in order to generate a smooth displacement curve. The phase offset of displacement is defined as the percent stride location where maximum displacement occurs on this smoothed curve. As an example, if we observe a value of 90 for phase offset it indicates that the peak lateral displacement occurs at the point where a stride cycle is 90% complete. The lateral displacement metric assigned to stride is the difference between maximum displacement value and minimum displacement value observed during a stride (Figure 3 A). This analysis is very sensitive and allows is detect subtle, but highly significant difference is overall posture during a stride (Video S4, S5, S6). We used the previous classical spatiotemporal measures based on Hildebrand's methods with the combined whole body posture metrics for our analysis. Because of the cyclic nature of phase offset metrics, care was taken to apply circular statistics to these in our analysis. The other measures are analyzed using linear methods.

3.4 Statistical Analysis and genetic validation of gait measures

Following gait and posture extraction, we established a statistical framework for analysis of the data. In order to validate our methods, we phenotyped three mouse models that have previously been shown to have gait defects and are preclinical models of human diseases - Rett's syndrome, Amyotrophic Lateral Sclerosis (ALS or Lou Gehrig's Disease), and Down syndrome. The three models, *Mecp2* knockout, SOD1 G93A transgene, and *Ts65Dn Trisomic*, respectively, were tested with appropriate controls at two ages in an one hour open field assay (Table 2). Gait metrics are highly correlated with animal size and speed of stride [45] (Figure 2I, J). However in many cases a change in stride speed is a defining feature of gait change due to genetic or pharmacological perturbation. In addition, we have multiple repeated measurements that are collected for each subject (mouse) and each subject has a different number of (strides) giving rise to imbalanced data. Averaging over repeated strides, which yields one average value per subject, can be misleading as it removes variation and introduces false confidence. At the same time, classical linear models do not discriminate between stable intra-subject variations and inter-subject fluctuations which severely bias the estimates. To

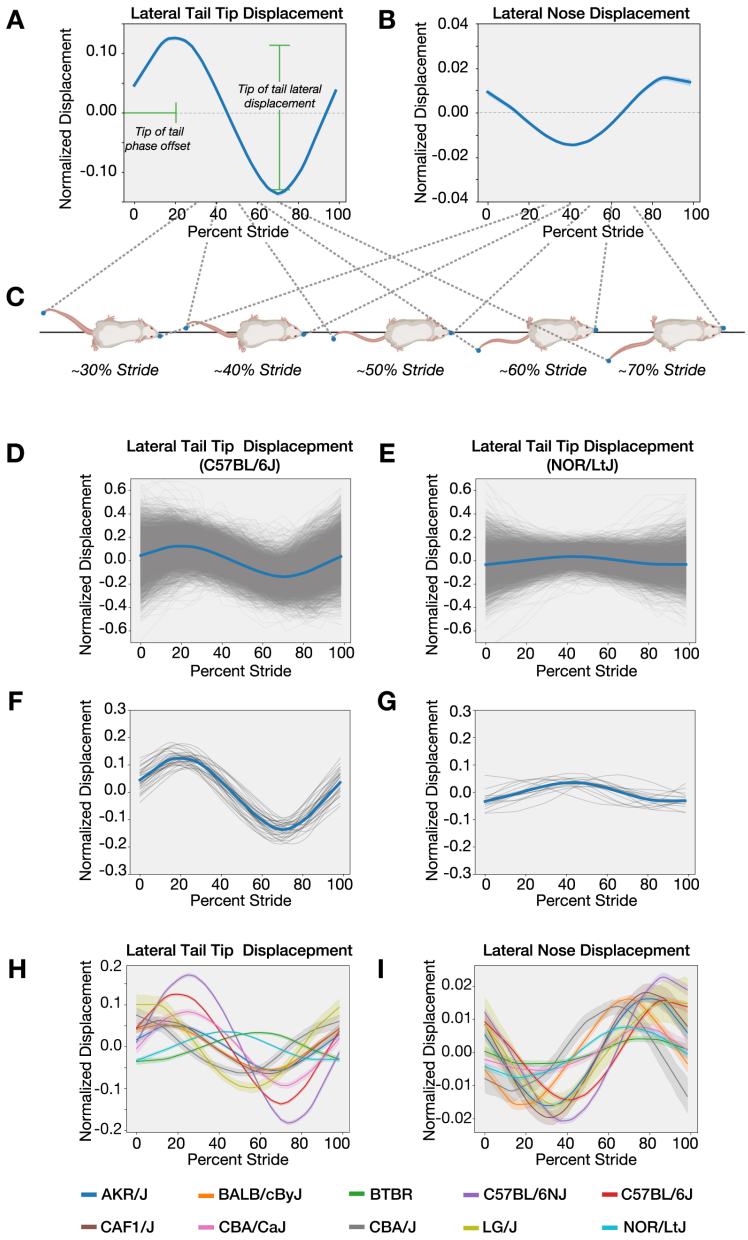

Figure 3: Extraction of cyclic whole body posture metrics during gait cycle. We measure lateral displacement of (A) the tail tip and (B) the nose. We can also average displacement across many strides within a cohort to form a consensus view such as (D) C57BL/6J vs. (E) NOR/LtJ or we can average many strides within individuals: (F) C57BL/6J vs. (G) NOR/LtJ. For tail (H) and nose (I) we see the diversity of lateral displacement between a set of strains selected from our strain survey. The translucent bands for these two plots represent the 95% confidence interval of the mean for each respective strain.

Measure	Definition of Measure	Units
Angular Velocity	The current angle of a mouse is determined by the vector connecting the mouse's base of tail to its base of neck. The first derivative of this value gives us angular velocity. For strides, angular velocity is averaged over the duration of the stride.	degrees/sec
Speed	The speed of a mouse is determined by tracking the movement speed of the base of tail keypoint. Stride speed is the average speed for all frames over the duration of a stride.	cm/sec
Limb Duty Factor	The stance time of a paw (the amount of time that the paw is in contact with the ground) divided by the full stride time. Duty factor is calculated for each of the hind paws and averaged.	None
Step Length	The distance that the right hind paw travels past the previous left hind paw strike	cm
Step Width	The averaged lateral distance separating hind paws. This is calculated as length of the shortest line segment that connects the right hind paw strike to the line that connects the left hind paw's toe-off location to its subsequent foot strike position.	cm
Stride Length	The full distance that the left hind paw travels for a stride, from toe-off to foot-strike.	cm
Lateral Displacement of Nose	In order to calculate lateral displacement, we first calculate the mouse's displacement vector for a stride. We then measure the nose's perpendicular distance from this vector for each frame of a stride. We now subtract the minimum distance from the maximum and divide by the mouse's body length so that the displacement measured in larger mice will be comparable to the distance measured in smaller mice.	None
Lateral Displacement of Base Of Tail	Calculated using the same approach which is applied to the Nose Lateral Displacement except that we are using the Base of Tail keypoint.	None
Lateral Displacement of Tip of Tail	Calculated using the same approach which is applied to the Nose Lateral Displacement except that we are using the Tip of Tail keypoint.	None
Nose Lateral Displacement Phase Offset	First, the lateral displacement is calculated for each frame of a stride as described for Nose Lateral Displacement above. We then perform a cubic spline interpolation in order to generate a smooth curve for displacement. We then determine the point in time where maximum displacement occurs. Note that because of cubic interpolation this can occur at time points between frames.	Percent Stride Cycle
Base of Tail Displacement Phase Offset	Calculated using the same approach which is applied to the Nose Lateral Displacement Phase Offset except that we are using the Base of Tail keypoint.	Percent Stride Cycle
Tip of Tail Displacement Phase Offset	Calculated using the same approach which is applied to the Nose Lateral Displacement Phase Offset except that we are using the Tip of Tail keypoint.	Percent Stride Cycle

Table 1: Gait metrics definitions.

address this, we used a linear mixed model (LMM) to dissociate within-subject variation from genotype-based variation between subjects [47, 48]. Specifically, in addition to the main effects such as animal size, genotype, age, a random effect that captures the intra-subject variation is included. Finally, we have multiple repeated measurements at two different ages giving rise to a nested hierarchical data structure. The models (M1, M2 M3) follow the standard LMM notation with (Genotype, BodyLength, Speed, TestAge) denoting the fixed effects and (MouseID/TestAge) (test age nested within the animal) denoting the random effect. In order to compare our results with previously published data that do not take animal size and sometimes speed of stride into account, we statistically modeled our results with three models that only take age and body length (M1), age and speed (M2), age, speed, and body length (M3) (Figure 4 and S1).

$$\text{M1} : \text{Phenotype} \sim \text{Genotype} + \text{TestAge} + \text{BodyLength} + (1 \mid \text{MouseID}/\text{TestAge})$$

$$\text{M2} : \text{Phenotype} \sim \text{Genotype} + \text{TestAge} + \text{Speed} + (1 \mid \text{MouseID}/\text{TestAge})$$

$$\text{M3} : \text{Phenotype} \sim \text{Genotype} + \text{TestAge} + \text{Speed} + \text{BodyLength} + (1 \mid \text{MouseID}/\text{TestAge})$$

We do not include sex in our models as it is highly correlated with body length (measured using ANOVA and denoted by η, is strong for both SOD1 ($\eta = 0.81$) and *Ts65Dn* ($\eta = 0.16$ overall, $\eta = 0.89$ for controls, $\eta = 0.61$ for mutants). We analyze *Mecp2* males and females separately. We model the circular phase variables in Table 1 as a function of linear variables using a circular-linear regression model [49]. To adjust for linear variables such as body length and speed, we include them as covariates in the model (also see Methods). We report p-values and normalized effect size in Figures 4, 5. For clarity, exact statistics are reported in detail in the supplementary tables S1, S2.

3.4.1 Validation using a Rett syndrome model

Rett syndrome, an inherited neurodevelopmental disorder, is caused by mutations in the X-linked *MECP2* gene [50]. We tested a commonly studied deletion of *Mecp2* that recapitulates many of the features of Rett syndrome, including reduced movement, abnormal gait, limb clasping, low birth weight, and lethality [51]. We tested hemizygous males ($n = 8$), heterozygous females ($n = 8$), and littermate controls ($n = 8$ of each sex) (Table 2). Null males are normal at birth and have an expected lifespan of about 50-60 days. They start to show age-dependent phenotypes by 3-8 weeks and lethality by 10 weeks. Heterozygous females have mild symptoms at a much older age [51]. We tested male mice twice at 43 and 56 days and females at 43 and 86 days.

Studies of this knockout have shown changes in stride length and stance width in an age-dependent manner in hemizygous males [52–54]. Recent analysis showed increased step width, reduced stride length, changes in stride time, step angle, and overlap distance [55]. However, these studies did not adjust for the reduced body size seen in *Mecp2* hemizygous males (Table 4) and in some cases did not model speed of the stride. The most relevant comparison of our data to previously published data is using M2, which models speed but not body length (Gadalla *et al.* [55], Table 4B). We find most of the gait metrics and several body coordination metrics are significantly different in the hemizygous males versus controls including limb duty factor, step and stride length, step width and temporal symmetry. However, most gait metrics are dependent on the size of the animal and the hemizygous males are 13% smaller in body length (Table 4) [51]. In addition, we limit our analysis to stride speeds between 20-30cm/s which allows us to reduce variation introduced by differences in speed. Therefore, we also compared a model that includes body length instead of speed as a covariate (M1, Figure 4A) and one in which both body length and speed are included (M3, Figure S1A). Results of M2 model indicated significant difference in stride speed, step width, stride length, whole body coordination phenotypes (tail tip amplitude, phase of tail tip and nose) in hemizygous males (Figure 4B). Most phenotypes were dependent on age with severe effects in males by 7 weeks (56 days) (Figure 4D). The model that includes both speed and body length (M3) showed a significant decrease in step width and suggestive difference in stride length, and robust differences in whole body coordination metrics (tail tip

amplitude, phase of tail tip, tail base, and nose) (Figure S1). We observed very few significant differences in *Mecp2* heterozygous females that are consistent across all three models. All three models consistently find tail tip amplitude to be significantly higher suggesting more lateral movement in the females (Figure 4A,B and S1). Combined, these results demonstrate that we are able to accurately detect previously described differences in *Mecp2*. In addition, our whole body coordination metrics are able to detect differences that have not been previously described.

3.4.2 Validation using an ALS model

Mice carrying the SOD1-G93A transgene are a preclinical model of ALS with progressive loss of motor neurons [56, 57]. The SOD1-G93A model has been shown to have changes in gait phenotypes, particularly of hindlimbs [58–64]. The most salient phenotypes are an increase in stance time (duty factor), and decreased stride length in an age-dependent manner. However, several other studies have observed opposite results [58, 59, 62, 63], and some have not seen significant gait effects [65]. These studies did not adjust for body size difference or in some cases for speed. We tested SOD1-G93A transgenes and appropriate controls at 64 and 100 days, during time of disease onset [58, 60, 63, 64, 66].

Surprisingly, we found that the phenotypes differing between transgene carriers and controls varied considerably depending on the linear mixed model used. M1, which adjusts for body length and age but not speed, finds stride speed, length, and duty factor as significantly different (Figure 4A). However, when speed is in the model (M2) or speed and body length are in the model (M3), the only differences are small changes in phase of tail tip and nose (Figure 4B and S1). This indicates that the changes seen in duty factor and stride length using M1 are due to changes in speed of the strides. These results argue that the major effect of the SOD1 transgene is on stride speed, which leads to changes in stride time and duty factor. Slight changes in whole body coordination are due to decrease in body size (Table 4). Our results are congruent with reports that gait changes may not be the most sensitive preclinical phenotype in this ALS model, and other phenotypes such as visible clinical signs and motor learning tasks such as rotarod are more sensitive measures [62, 65]. In sum, our results validate the statistical model and may help explain some of the discordant results in the literature.

3.4.3 Validation using a Down syndrome model

Down syndrome, caused by trisomy of all or part of chromosome 21, has complex neurological and neurosensorial phenotypes [67]. Although there are a spectrum of phenotypes such as intellectual disability, seizures, strabismus, nystagmus, and hypoacusis, the more noticeable phenotypes are developmental delays in fine motor skills [68, 69]. These are often described as clumsiness or uncoordinated movements [70, 71]. One of the best studied models, Tn65Dn mice are trisomic for a region of mouse chromosome 16 that is syntenic to human chromosome 21 and recapitulate many of the features of Down syndrome [72, 73]. Tn65Dn mice have been studied for gait phenotypes using traditional inkblot footprint analysis or treadmill methods [74–76]. The inkblot analysis showed mice with shorter and more "erratic" and "irregular" gait, similar to motor coordination deficits seen in patients [75]. Treadmill-based analysis revealed further changes in stride length, frequency, some kinetic parameters, and foot print size [76, 77]. These previous analyses have not studied the whole body posture of these mice.

We analyzed Tn65Dn mice along with control mice at approximately 10 and 14 weeks (Table 2) and all three linear mixed models M1-M3 found consistent changes. The Ts65Dn mice are not hyperactive in the open field (Figure 4C), although they have increased stride speed (Figures 4A, C). This indicates that the Tn65Dn mice take quicker steps but travel the same distance as controls. Step width was increased and step and stride lengths were significantly reduced. The most divergent results from controls are obtained with M3,

which accounts for speed and body length. In particular, whole body coordination phenotypes were highly affected in the Tn65Dn mice. The amplitude of tail base and tip, and the phase of tail base, tip, and nose were significantly decreased (Figure S1A). We confirmed this with a phase plot of nose and tail tip (Figure 4E). Surprisingly, we found that there were large differences in phase. The tail tip phase peak is near 30% of the stride cycle in controls and close to 60% in mutants at multiple speeds (Figure 4E). Similar changes are seen in the phase plot for the nose. Combined, these results confirm previous reported differences in traditional gait measures, and highlight the utility of our novel open field whole body coordination measures in broadening the assayable phenotypic features in models of human disease. Indeed, the most salient feature of the Tn65Dn gait is the alteration of whole body coordination which previously was reported as a qualitative trait using inkblot analysis [75] and is now quantifiable using our methods.

3.5 Characterization of autism spectrum disorder-related mutants

To further validate our approach, we investigated gait in four autism spectrum disorder (ASD) mouse models, in addition to *Mecp2* above that also falls on this spectrum. In humans, gait and posture defects are often seen in ASD patients and sometimes gait and motor defects precede classical deficiencies in verbal and social communication and stereotyped behaviors [5, 6]. Recent studies indicate that motor changes are often undiagnosed in ASD cases [78]. It is unclear if these differences have genetic etiologies or are secondary to lack of social interactions that may help children develop learned motor coordination [79]. In mouse models of ASD, gait defects have been poorly characterized, and thus we sought to determine if any gait phenotypes occur in four commonly used ASD genetic models, which we characterized with appropriate controls at 10 weeks (Table 3). Similar to the three models with known gait defects, we tested these mutants and controls in the one hour open field assay and extracted gait and posture metrics (Table 1). We modeled the results using the same approach used for gait mutants (M1 and M3 results are presented in Figure 5, M2 results are in Figure S2).

Cntnap2 is a member of the neurexin gene family which functions as a cell adhesion molecule between neurons and glia [80]. Mutations in *Cntnap2* have been linked to neurological disorders such as ASD, schizophrenia, bipolar disorder, and epilepsy [81]. *Cntnap2* knockout mice have previously been shown to have mild gait effects, with increased stride speed leading to decreased stride duration [82]. We used model M2 to compare our results to the previous study and found that *Cntnap2* mice show significant differences in a majority of the gait measures (Figure S2). These mice are significantly smaller in body length and weight than controls (Table 4, Figure S2C). In the open field, *Cntnap2* mice were not hyperactive (Figure 5C) but showed a markedly increased stride speed (M1, Figure 5A, C and Figure S2C). These results argue that the *Cntnap2* mice do not travel more, but take quicker steps when moving, similar to Ts65Dn mice.

Since *Cntnap2* mice are smaller and have faster stride speeds, we used results from M3 to determine if gait parameters are altered after adjusting for body size and stride speed (Table 4). We found that *Cntnap2* mice were significantly different from controls for a majority of the traditional gait metrics as well as whole body coordination measures in both models M1 and M3 (Figure 5B). The *Cntnap2* mice have reduced limb duty factor, step length, step width, and highly reduced stride length (Figure 5 B, D and S2). The mice also show altered phase of tail tip, base, and nose, as well as significant but small changes in amplitude of tail tip base and nose. Another salient feature of gait in *Cntnap2* mice is the decrease in inter-animal variance compared to controls, particularly for limb duty factor (Fligner-Killeen test, $p < 0.01$), step length (Fligner-Killeen test, $p < 0.01$), and stride length (Fligner-Killeen test, $p < 0.02$) (Figure 5D). This may indicate a more stereotyped gait in these mutants. Combined, these results imply that *Cntnap2* mice are not hyperactive as measured by total distance traveled in the open field, but are hyperactive at the individual stride level. They take quicker steps with shorter stride and step length, and narrower step width. Finally, we attempted to distinguish *Cntnap2* mice from controls based on all combined gait measures using unsupervised clustering. We first performed a principal component analysis (PCA) on the linear gait phenotypes and then used Gaussian

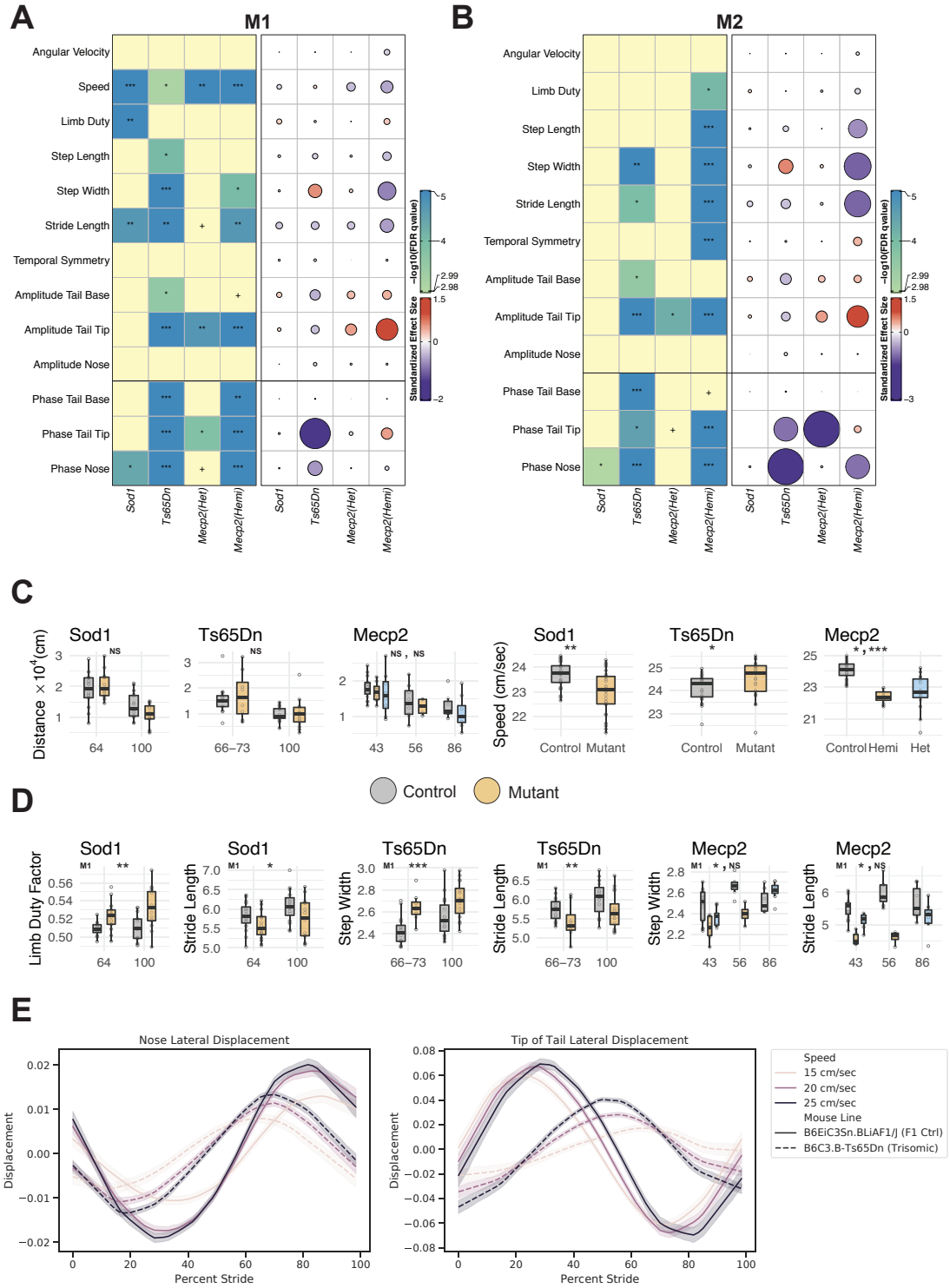

Figure 4: Method validation using genetic gait mutants. (A) q-values (left columns) and effect sizes (right columns) for the effect of Genotype obtained from model M1 for linear phenotypes and circular-linear models for circular phenotypes. (B) Same as (A) except that the model used is M2 for linear phenotypes. (C) Total distance covered and speed are compared between controls and mutants using linear and linear mixed models respectively adjusting for body length and age. (D) Body length-adjusted gait metrics that were found to be different for linear mixed effects model. (E) Lateral displacement of nose and tail tip for Ts65Dn strain. The solid lines represent the mean displacement of stride while the translucent bands provides a 95% confidence interval for the mean.

mixture modeling (GMM) on the PCs to cluster the animals into two separate groups. We found that the gait metrics allow us to distinguish *Cntnap2* from controls (Figure 5E). This analysis argues that *Cntnap2* mice can be distinguished from controls based on its gait patterns in the open field, and that these phenotypes are more dramatic than previously detected [82].

Mutations in *Shank3*, a scaffolding postsynaptic protein, have been found in multiple cases of ASD [83]. Mutations in *Fmr1*, a RNA binding protein that functions as a translational regulator, are associated with Fragile X syndrome, the most commonly inherited form of mental illness in humans [84]. Fragile X syndrome has a broad spectrum of phenotypes that overlaps with ASD features [85]. *Del4Aam* mice contain a deletion of 0.39Mb on mouse chromosome 7 that is syntenic to human chromosome 16p11.2 [86]. Copy number variations (CNVs) of human 16p11.2 have been associated with a variety of ASD features, including intellectual disability, stereotypy, and social and language deficits [87]. *Fmr1* mutant mice travel more in the open field (Figure 5C) and have higher stride speed (Figures 5A, C). When adjusted for stride speed and body length (M3) these mice have slight but significant changes in limb duty factor in M2 and M3. *Shank3* and *Del4Aam* are both hypoactive in the open field compared to controls. *Shank3* mice have a significant decrease in stride speed, whereas *Del4Aam* mice have faster stride speeds (5A, C). All three statistical models show a suggestive or significant decrease in step length in both strains. Using M3, we find that *Shank3* have longer step and stride length, whereas *Del4Aam* have shorter steps and strides. In whole body coordination, *Shank3* mice have a decrease in nose phase and *Del4Aam* has an increase in tail tip phase. These results indicate that, even though both *Shank3* and *Del4Aam* are hypoactive in the open field, *Shank3* takes slower and longer strides and steps, whereas *Del4Aam* takes faster strides with shorter steps and strides. Both mutants have some defects in whole body coordination. In sum, we find each of the ASD models to have some gait deficits, with *Cntnap2* having the strongest phenotypes. All have some change in stride speed, although the directionality of change and the variance of the phenotype differ.

3.6 Strain Survey

After validation of our methods, we sought to understand the range of gait and posture phenotypes in the open field in standard laboratory mouse strains. We surveyed 44 classical inbred laboratory strains, 7 wild derived inbred strains, and 11 F1 hybrid strains (1898 animals, 1,740 hours of video). All animals were isogenic and we surveyed both males and females in a one hour open field assay (Table 5) [37]. We then extracted gait metrics from each video and analyzed the data on a per-animal level (Figure 6A,B, S3, S4). We analyzed stride data when animals were traveling in medium speed (20 to 30 cm/sec) and in a straight direction (angular velocity between -20 to +20 degrees/sec). We could carry out such a selective analysis because of the large amount of data we were able to collect and process in freely moving mice. Since these mice vary considerably in their size, we used residuals from M1 that adjusts for body size [37]. M1 allows us to extract stride speed as a feature, which we found to be important in ASD mutants. In order to visualize differences between strains, we calculated a z-score for each strain's phenotype and carried out k-means clustering (Figure6 B). Overall, we observed high inter-strain variability in most of the classical gait and whole body posture metrics, indicating high levels of heritability of these traits. We also observed emerging patterns in open field gait movements of laboratory mouse with certain strains showing similar behaviors.

We sought to determine if we could cluster strains based on their open field gait and posture phenotypes. We applied a k-means clustering algorithm on the principal components obtained by performing a PCA on the original linear gait features, as we did for the *Cntnap2* mutant. We did not include circular phase metrics in our clustering analysis as both PCA and k-means clustering algorithms assume the metrics to lie in a Euclidean space. We picked the first 2 PCs as they explain 53% of the total variance in the original feature space. We looked at four criteria to assess the quality of clustering and chose the optimal number of clusters in our k-means clustering algorithm, all of which indicated 3 optimal clusters (Figure S5). We find that there are three clusters of strains that can be distinguished based on their open field gait behaviors (Figure 6C, D,

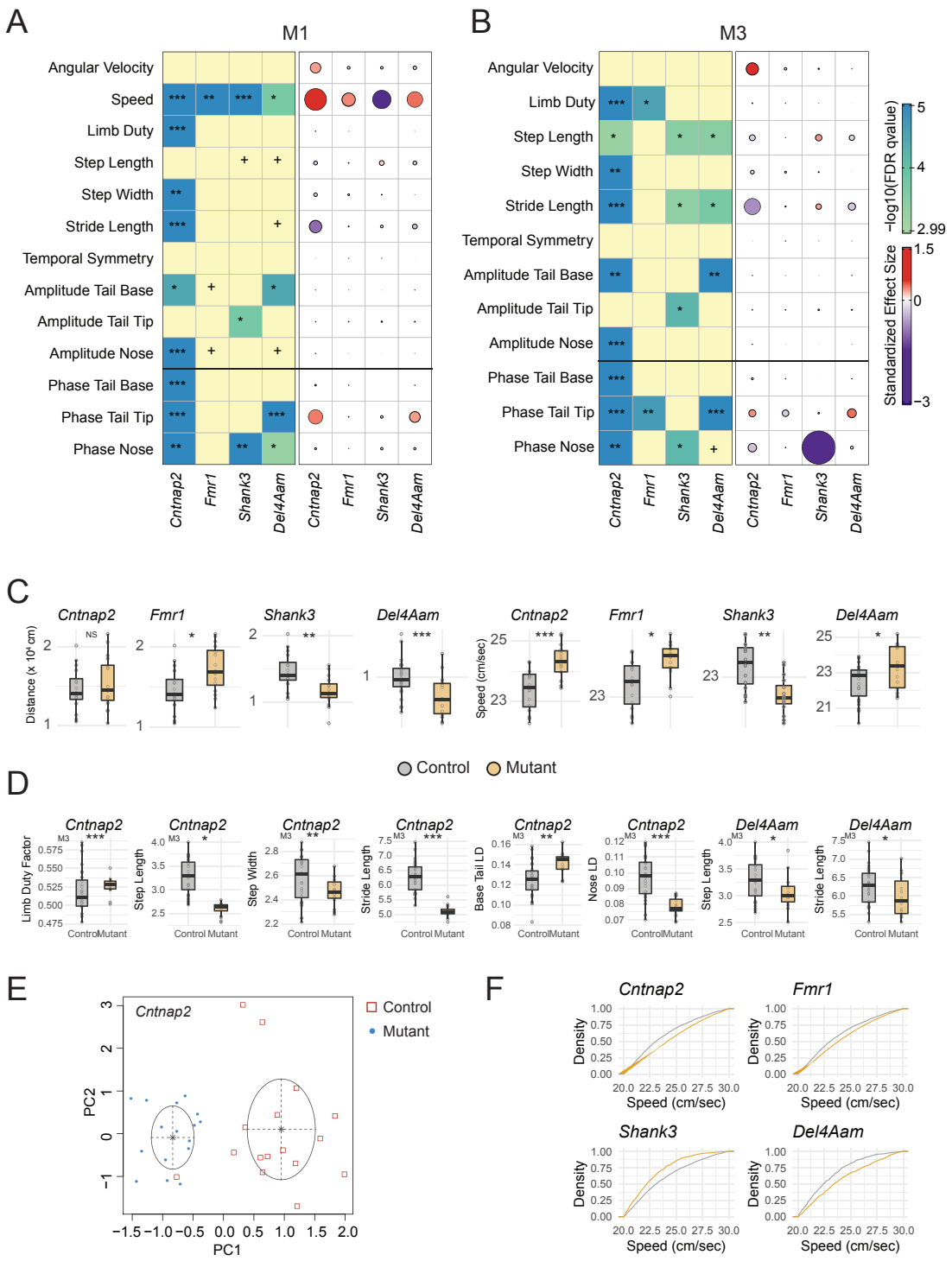

Figure 5: Characterization of gait and posture in mouse genetic models of autism. (A) q-values (left) and effect sizes (right) for the effect of Genotype obtained from model M1 for linear phenotypes and circular-linear models for circular phenotypes. (B) q-values (left) and effect sizes (right) obtained from model M3 for linear phenotypes and circular-linear models for circular phenotypes.(C) Total distance covered and speed are compared between controls and mutants using linear and linear mixed models respectively adjusting for body length and age. (D) Body length-adjusted gait metrics that were found to be different for linear mixed effects model. (E) We use the first two principal components to build a 2D representation of the multidimensional space in which controls and mutants are best separated. (F) Cumulative distribution plots of speed are plotted for comparison between controls and mutants.

E). Cluster 1 consists of mostly classical strains such as A/J, C3H/HeJ, 129S1/SvImJ; cluster 2 consists of several classical strains and a large number of wild derived strains such as MOLF/EiJ and CAST/EiJ. Cluster 3 mainly consists of C57 and related strains, including the reference C57BL/6J. We constructed a consensus stride phase plot of the nose and tail tip for each cluster. Cluster 3 has much higher amplitude, while clusters 1 and 2 have similar amplitude but shifted phase offset (Figure 6D). An examination of the linear gait metrics reveals individual metrics that distinguish the clusters (Figure 6E). For example, cluster 1 has longer stride and step length, while cluster 3 has higher lateral displacement of tail base and tip, while cluster 2 has low lateral displacement of nose. Overall an analysis of individual metrics reveal a significant difference in 9 of 11 measures. Combined, this analysis reveals high levels of heritable variation in gait and whole body posture in the laboratory mouse. A combined analysis using multidimensional clustering of these metrics finds three subtypes of gait in the laboratory mouse. Our results also show that the reference mouse strain, C57BL/6J, is distinct from other common mouse strains and wild derived strains.

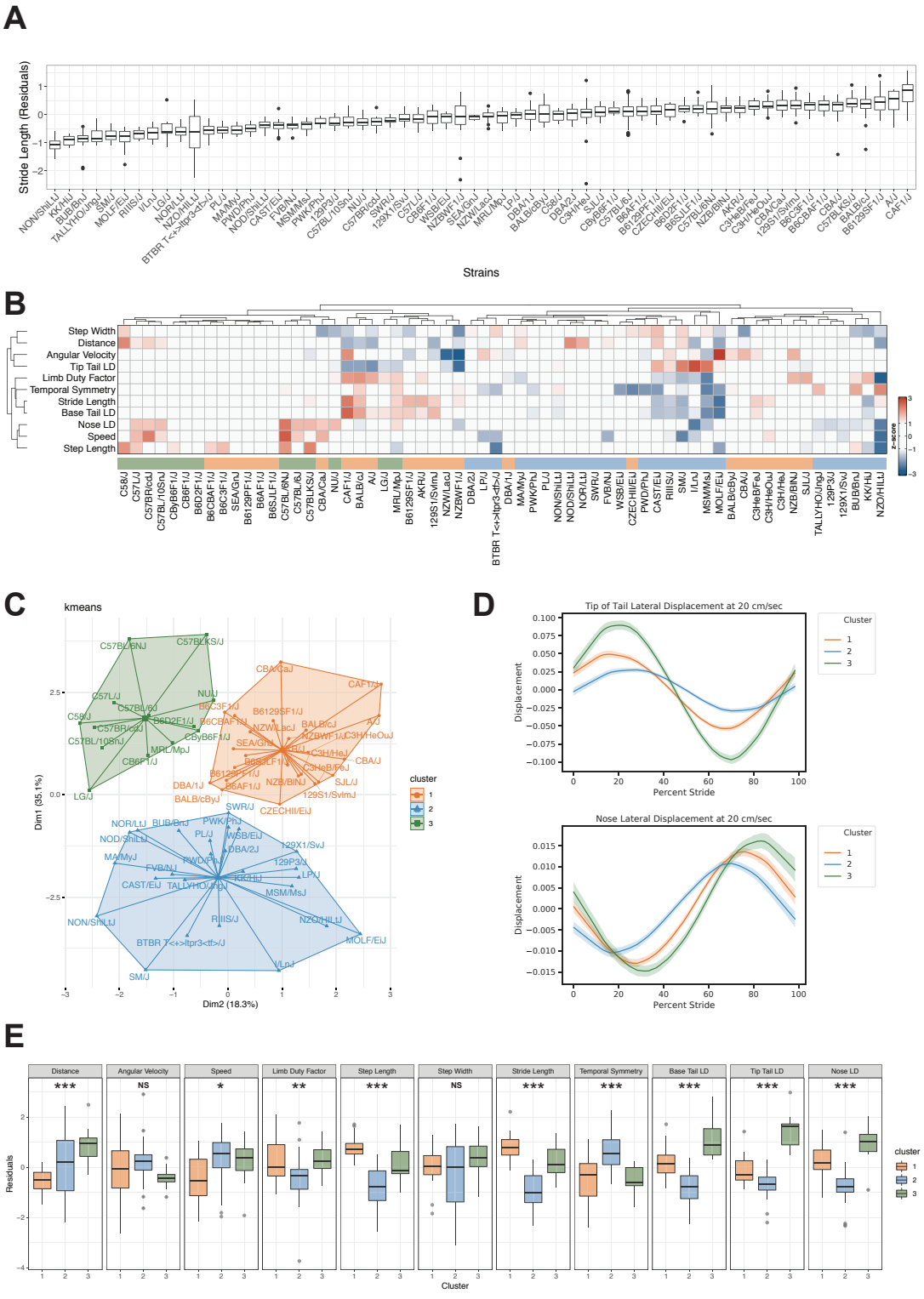

Figure 6: (A) Each boxplot corresponds to a strain, with vertical position indicating residuals of stride length-adjusted for body length. Strains are ordered by their median residual stride length value. (B) z-scores of body length adjusted gait metrics for all strains color-coded by the cluster membership (see (C)). (C) We use K-means algorithm to build, using the first two principal components, a 2D representation of the multidimensional space in which strains are best separated. (D) A consensus view of lateral displacement of nose and tail tip across the clusters. The solid lines represent the mean displacement of stride while the translucent bands provide a 95% confidence interval for the mean. (E) Post-clustering plots summarizing the residual gait metrics across different clusters.

3.7 GWAS

The strain survey demonstrated that the gait features we measure are highly variable, and we thus wanted to understand the heritable components and the genetic architecture of mouse gait in the open field. In human GWAS, both mean and variance of gait traits are highly heritable [88]. We separated the strides of each animal into four different bins according to the speed it was travelling (10-15, 15-20, 20-25, and 25-30 cm/s) and calculated mean and variance of each trait for each animal in order to conduct a GWAS to identify Quantitative Trait Loci (QTL) in the mouse genome. We used GEMMA [89] to conduct a genome wide association analysis using a linear mixed model, taking into account sex and body length as fixed effects, and population structure as a random effect. Since linear mixed models do not handle circular values, we excluded phase gait data from our analysis. The heritability was estimated by determining the proportion of variance of a phenotype that is explained by the typed genotypes (PVE) (Figure 7A left panel). Heritability of gait measures showed a broad range and the majority of the phenotypes are moderately to highly heritable. The mean phenotypes with lowest heritability are angular velocity and temporal symmetry, indicating that variance in the symmetrical nature of gait or turning behaviors are not due to genetic variance in the laboratory mouse. In contrast, we find that measures of whole body coordination (amplitude measures) and traditional gait measures are moderately to highly heritable. Variance of phenotypes showed moderate heritability, even for traits with low heritability of mean traits (Figure 7A right panel). For instance, mean AngularVelocity phenotypes have low heritability (PVE < 0.1), whereas the variance AngularVelocity phenotypes have moderate heritability (PVE between 0.25 - 0.4). These heritability results indicated that the gait and posture traits are appropriate for GWAS of mean and variance traits.

For significance threshold, we calculated an empirical p-value correction for the association of a SNP with a phenotype by shuffling the values (total distance traveled in the open field) between the individuals 1000 times. In each permutation, we extracted the lowest p-value to find the threshold that represents a corrected p-value of 0.05 (1.9×10^{-5}). We took the minimal p-value over all mean phenotypes, variance phenotypes, and both classes combined for each SNP to generate combined Manhattan plots (Figure 7B-D). Each SNP is colored according to the phenotype associated to the SNP with the lowest p-value. The different speed bins were usually consistent for each phenotype and we decided to combine all bins of the same phenotype by taking the minimal p-value of the four bins for each SNP.

We found 239 QTL for mean traits and 239 QTL for variance traits (Figure 7B-C). The least heritable phenotype, mean AngularVelocity, showed only one significant associated genomic region, whereas the variance of AngularVelocity had 53 associated genomic loci. The phenotype with the most associated loci was stride count with 95 loci. Overall, when considering all the phenotypes together, we found 400 significant genomic regions associated with at least one phenotype (Supp. Table 3), indicating only 78 QTL were identified for both a mean phenotype and a variance phenotype. Most phenotypes had limited to no overlap between QTL associated with the mean of the feature and its variance. Of note, QTL associated with mean TemporalSymmetry and variance TemporalSymmetry had a lot of overlapping regions. Out of 28 loci associated with the mean phenotype and 52 with variance, ten QTL overlapped. These data argue that the genetic architecture of mean and variance traits in the mouse are largely independent. These results also begin to outline the genetic landscape of mouse gait and posture in the open field.

4 Discussion

Gait and posture are an important indicator of health and are perturbed in many neurological, neuromuscular, and neuropsychiatric diseases. The goal of this project was to develop a simple and reliable automated system that is capable of performing pose estimation on mice and to extract key gait and posture metrics from pose. We present a solution that allows researchers to adapt a video imaging system used for open field analysis

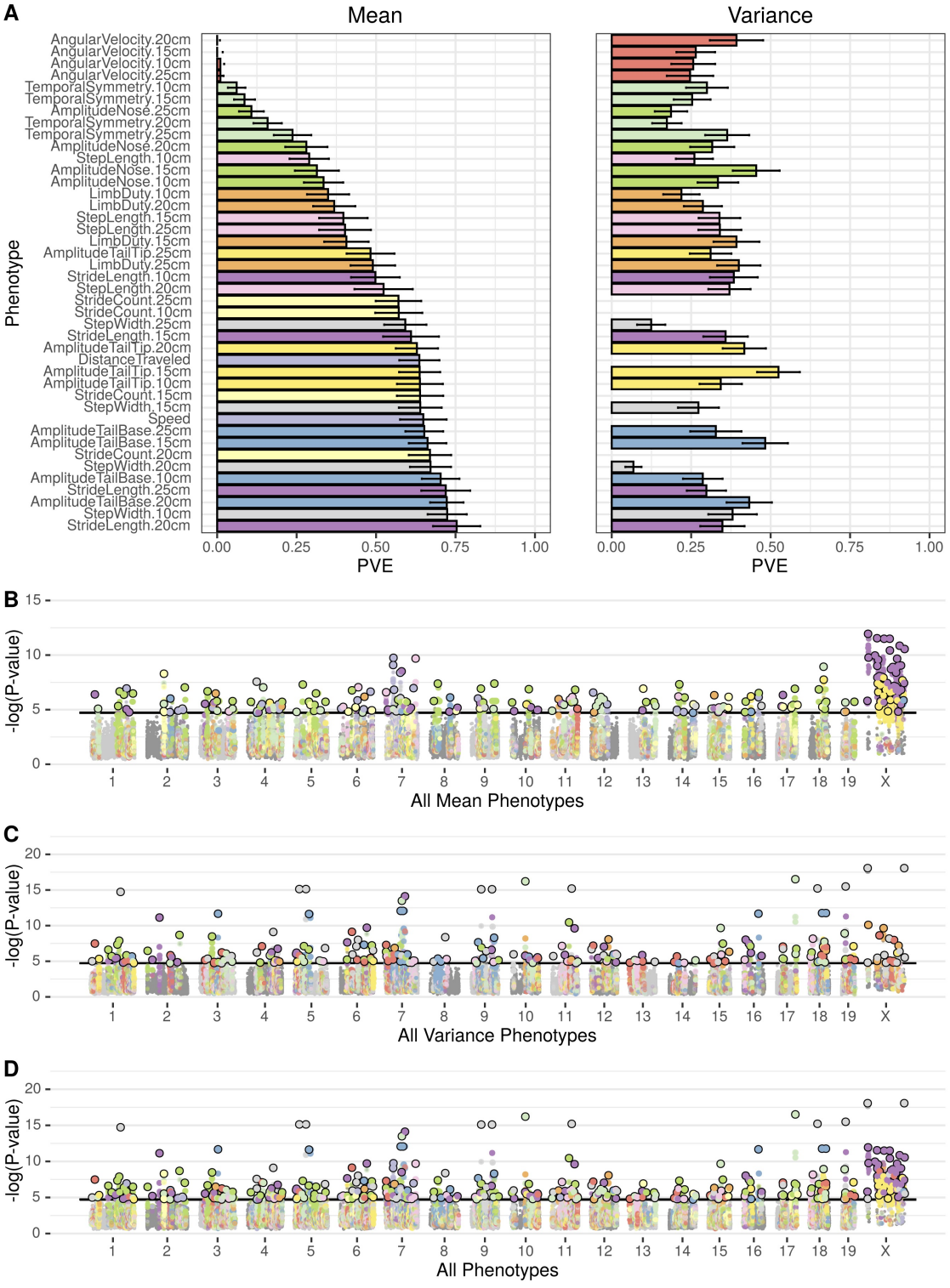

Figure 7: GWAS results for gait phenotypes. (A) Heritability estimates for each phenotype mean (left) and variance (right). (B-D) Manhattan plots of all mean phenotypes (B), variance phenotypes (C), and all of them combined (D); colors correspond to the phenotype with the lowest p-value for the SNP.

to extract gait metrics. Our approach has some clear advantages and limitations. We are able to process a large amount of data with low effort and low cost since the only data that needs to be captured is top-down gray scale video of a mouse in an open field, and all pose estimation and gait metric extraction is fully automated after that. Because our method does not require expensive specialized equipment, we can also allow the mouse time to acclimate to the open field and collect data over long periods of time. Additionally our method allows the animal to move of its own volition (unforced behavior) in an environment which is familiar to it, a more ethologically relevant assay [28]. One limitation of our approach is that we cannot measure kinetic properties of gait because we are limiting ourselves to video [23] . The decision to use top-down video also means that some pose keypoints are often occluded by the mouse's body. The pose estimation network is robust to some amount of occlusion as is the case with the hind paws but the forepaws, which are almost always occluded during gait, have pose estimates which are too inaccurate and so have been excluded from our analysis. Regardless, in all genetic models that we tested, hind paw data is sufficient to detect robust differences in gait and body posture. In addition, the ability to analyze large amounts of data in free moving animals, proves to be highly sensitive, even with very strict heuristic rules around what we consider to be a gait.

The gait measures we extract are commonly quantified in experiments (e.g. step width and stride length), but measures of whole body coordination such as lateral displacement and phase of tail are typically not measured in rodent gait experiments (phase and amplitude of keypoints during stride). Gait and whole body posture is frequently measured in humans as an endophenotype of psychiatric illness sanders2010gait, licari2020prevalence, flyckt1999neurological, walther2012motor. Our results in mice indicate that gait and whole body coordination measures are highly heritable and perturbed in disease models. Specifically, we test neurodegenerative (*Sod1*), neurodevelopmental (Down syndrome, *Mecp2*) and ASD models (*Cntnap2, Shank3, FMR1, Del4Am*) and find altered gait features in all of these mutants. Others have also found similar results with neurodegerative models machado2015quantitative. Of note are the data for Down syndrome. In humans, miscoordination and clumsiness are prominent features of Down syndrome. In mouse models, this miscoordination was previously characterized in ink blot gait assays as a disorganized hind foot print. Here, our analysis revealed perturbed whole body coordination differences between control and Tn65Dn mice. Our approach thus enables quantitation of a previously qualitative trait.

Our analysis of a large number of mouse strains for gait and posture finds three distinct classes of overall movement. We find that the reference C57BL/6J and related strains belong to a distinct cluster separate from other common laboratory as well as wild-derived strains. The main difference is seen in the high amplitude of tail and nose movement of the C57BL/6 and related strains. This may be important when analyzing gait and posture in differing genetic backgrounds. The GWAS revealed 400 QTL for gait and posture in the open field for both mean and variance phenotypes. We found that the mean and variance of traits are regulated by distinct genetic loci. Indeed, we find most variance phenotypes show moderate heritability, even for mean traits with low heritability. Human GWAS have been conducted for gait and posture, albeit with under powered samples, which has lead to good estimates of heritability but only a few significantly associated loci adams2016heritability. Our results in the mouse argue that a well-powered study in humans may identify hundreds of genetic factors that regulates gait and posture.

5 Methods

5.1 Training Data

Labeled data consists of 8,910 480x480 grayscale frames containing a single mouse in the open field along with the twelve manually labeled pose keypoints per frame. We selected from a diverse set of mouse strain with different appearance accounting for variation in coat color, body size and obesity. Figure 2(C) shows a representative frame generated by our open field apparatus. The frames were generated from the same open field apparatus as was used to generate experimental data previously [37]. Pose keypoint annotations were performed by several Kumar lab members. Frame images and keypoint annotations were stored together using an HDF5 format which was used for neural network training. Frame annotations were split into a training dataset (7,910 frames) and a validation dataset (1,000 frames) for training.

5.2 Neural Network Training

We train our network over 600 epochs and perform validation at the end of every epoch. The training loss curves (figure 2 (C)) show a fast convergence of the training loss without an overfitting of the validation loss. We used transfer learning [90, 91] on our network in order to minimize the labeling requirements and improve the generality of our model. We started with the imagenet model provided by the authors of the HRNet paper (hrnet_w32-36af842e.pth) and froze the weights up to the second stage during training. In order to further improve the generality of our network we employed several data augmentation techniques during training including: rotation, flipping, scaling, brightness, contrast and occlusion. We use the ADAM optimizer to train our network. The learning rate is initially set to 5×10^{-4}, then reduced to 5×10^{-5} at the 400th epoch and 5×10^{-6} at the 500th epoch.

5.3 Statistical Analysis

We consider the following LMM model for repeated measurements:

$$\mathrm{y}_{ij} = \mathrm{x}_{ij}^{\mathrm{T}}\beta + \gamma_i + \epsilon_{ij}, \quad i = 1, \ldots, n, \;\; j = 1, \ldots, n_i$$

where n is the total number of subjects; y_{ij} is the jth repeat measurement on the ith subject, n_i denotes the number of repeat measurements on subject i; x_{ij} is a $p \times 1$ vector of covariates such as body length, speed, genotype, age; β is a $p \times 1$ vector of unknown fixed population-level effects; γ_i is a random intercept which describes subject-specific deviation from the population mean effect; and ϵ_{ij} is the error term that describes the intrasubject variation of the ith subject that is assumed to be independent of the random effect. To test fixed effects and get p-values, we use the F test with Satterthwaite's approximation to the denominator degrees of freedom. We fit our LMM models using the lme4 package in R [92]. We did not include sex in our models where it is highly correlated with body length.

We model the circular phase variables in Table 1 as a function of linear variables using a circular-linear regression model. Analyzing circular data is not straightforward and statistical models developed for linear data do not apply to circular data [93]. The circular response variables are assumed to have been drawn from a von-Mises distribution with unknown mean direction μ and concentration parameter κ. The mean direction parameter is related to the variables $\mathbf{X}$ through the equation

$$Y_i \sim \text{von Mises}(\mu_i, \kappa), \quad \mu_i = \mu + g(\gamma_1 X_1 + \ldots + \gamma_p X_p), \quad i = 1, \ldots, n$$

where $g(u) = 2\tan^{-1}(u)$ is a link function such that for $-\infty < u < \infty, -\pi < g(u) < \pi$. The parameters $\mu, \gamma_1, \ldots, \gamma_k$ and κ are estimated via maximum likelihood. The model is fitted using the circular package in R. [94]

5.4 Animals

Strain	JMCRS #	Genotype	Sex	Short Name	Control Strain
B6.129P2(C)-Mecp2$^{tm1.1Bird}$/J	003890	HEMI	M	Mecp2	Littermate WT
B6.129P2(C)-Mecp2$^{tm1.1Bird}$/J	003890	HET	F	Mecp2	Littermate WT
B6.Cg-Tg(SOD1*G93A)1Gur/J	004435	HEMI	M/F	Sod1	Littermate WT
B6EiC3Sn.BLiA-Ts(17^{16})65Dn/DnJ	005252	Trisomic	M/F	Ts65Dn	B6EiC3Sn.BLiAF1/J
B6EiC3Sn.BLiAF1/J	003647	F1	M/F		N/A

Table 2: Control strains and official identifiers for gait mutants.

Strain	JMCRS #	Short Name	Control Strain
B6.129P2-*Fmr1*^{tm1Cgr}/J	003025	*Fmr1*	C57BL/6J
B6129S-Del(7Slx1b-Sept1)4Aam/J	013128	*Del4Aam*	B6129SF1/J
B6.129-Shank3^{tm2Gfn}/J	017688	*Shank3*	C57BL/6J
B6.129(Cg)-Cntnap2^{tm1Pele}/J	028635	*Cntnap2*	C57BL/6J
B6129SF1/J	101043		N/A
C57BL/6J	000664		N/A

Table 3: Control strains and official identifiers for autism mutants.

Gait Mutants						
Strain	Sex	BodyLength (cm)		Correlation	BodyWeight (g)	
		Control	Mutant	r	Control	Mutant
Sod1	M	$6.16 \pm .15$	$6.23 \pm .26$	0.48	28.90 ± 2.69	26.41 ± 2.25
	F	$5.53 \pm .31$	$5.47 \pm .32$	0.76	21.74 ± 2.38	20.08 ± 1.84
Ts65Dn	M	$5.90 \pm .29$	$5.75 \pm .37$	0.73	30.46 ± 4.16	29.39 ± 6.39
	F	$5.55 \pm .24$	$5.77 \pm .42$	0.73	23.28 ± 2.20	25.51 ± 6.59
Mecp2	M	$5.69 \pm .23$	$4.82 \pm .31$	0.94	23.53 ± 1.77	15.68 ± 1.81
	F	$5.25 \pm .35$	$5.33 \pm .37$	0.91	19.31 ± 3.09	19.86 ± 3.27
Autism Mutants						
Cntnap2	M	$6.03 \pm .37$	$5.56 \pm .28$	0.72	28.28 ± 1.95	23.95 ± 1.71
	F	$5.65 \pm .25$	$5.41 \pm .29$	0.72	22.69 ± 2.05	19.40 ± 0.97
Fmr1	M	$6.03 \pm .37$	$6.17 \pm .20$	0.77	28.28 ± 1.95	29.49 ± 1.37
	F	$5.65 \pm .25$	$5.66 \pm .17$	0.47	22.69 ± 2.05	21.01 ± 1.12
Shank3	M	$6.03 \pm .37$	$6.00 \pm .11$	0.75	28.28 ± 1.95	28.24 ± 1.00
	F	$5.65 \pm .25$	$5.60 \pm .23$	0.70	22.69 ± 2.05	21.60 ± 1.70
Del4Aam	M	$6.42 \pm .36$	$6.18 \pm .51$	0.70	33.13 ± 3.21	23.22 ± 2.43
	F	$5.50 \pm .29$	$5.84 \pm .49$	0.70	21.29 ± 1.49	18.16 ± 2.32

Table 4: Summary data for body length and weight of animals in our experiments.

	Strain	N	Males	Females
1	129P3/J	23	8	15
2	129S1/SvlmJ	17	13	4
3	129X1/SvJ	15	8	7
4	A/J	6	4	2
5	AKR/J	17	9	8
6	B6129PF1/J	30	10	20
7	B6129SF1/J	24	15	9
8	B6AF1/J	35	17	18
9	B6C3F1/J	32	12	20
10	B6CBAF1/J	18	9	9
11	B6D2F1/J	22	12	10
12	B6SJLF1/J	28	5	23
13	BALB/cByJ	18	11	7
14	BALB/cJ	21	19	2
15	BTBR T<+>ltpr3<tf>/J	53	32	21
16	BUB/BnJ	15	7	8
17	C3H/HeJ	27	11	16
18	C3H/HeOuJ	19	6	13
19	C3HeB/FeJ	10	5	5
20	C57BL/10SnJ	19	10	9
21	C57BL/6J	494	298	196
22	C57BL/6NJ	293	126	167
23	C57BLKS/J	30	19	11
24	C57BR/cdJ	15	3	12
25	C57L/J	23	10	13
26	C58/J	11	7	4
27	CAF1/J	14	8	6
28	CAST/EiJ	33	10	23
29	CB6F1/J	27	18	9
30	CBA/CaJ	30	15	15
31	CBA/J	14	9	5
32	CByB6F1/J	18	14	4
33	CZECHII/EiJ	11	4	7
34	DBA/1J	27	12	15
35	DBA/2J	17	8	9
36	FVB/NJ	13	5	8
37	I/LnJ	14	6	8
38	KK/HiJ	8	5	3
39	LG/J	6	3	3
40	LP/J	25	15	10
41	MA/MyJ	15	7	8
42	MOLF/EiJ	9	3	6
43	MRL/MpJ	12	4	8
44	MSM/MsJ	11	3	8
45	NOD/ShiLtJ	25	13	12
46	NON/ShiLtJ	27	13	14
47	NOR/LtJ	13	7	6
48	NU/J	10	5	5
49	NZB/BlNJ	21	5	16
50	NZBWF1/J	17	9	8
51	NZO/HILtJ	14	6	8
52	NZW/LacJ	11	7	4
53	PL/J	12	4	8
54	PWD/PhJ	12	7	5
55	PWK/PhJ	9	5	4
56	RIIIS/J	10	3	7
57	SEA/GnJ	7	4	3
58	SJL/J	34	4	30
59	SM/J	12	8	4
60	SWR/J	12	2	10
61	TALLYHO/JngJ	22	13	9
62	WSB/EiJ	11	8	3

Table 5: Summary data for strain counts in the strain survey

6 Acknowledgements

We thank members of the Kumar Lab for helpful advice and Taneli Helenius for editing. This work was funded by The Jackson Laboratory Directors Innovation Fund, National Institute of Health DA041668 (NIDA) and DA048634 (NIDA). All code and training data will be available at Kumarlab.org and Kumar Lab Github.

7 Competing Interests

The authors have no competing interest.

8 Supplementary data not in pdf document

Video S1 - Examples of pose estimation. Pose estimation on visually diverse mouse strains using the architecture shown in Figure 1.

Video S2 - Gait extraction from pose estimation. The top panel shows a segment of video with a gait overlay similar to what is described in Figure 2C. The bottom panel contains two plots that update with the video: an angular velocity plot similar to Figure 2F and a hind paw speed plot as described in Figure 2D. Green bouts are considered strides, left and right paws are orange and blue respectively.

Video S3 - Aggregated stride cycles for the *Ts65Dn Trisomic* mouse model: individual stride cycle keypoints overlaid and rendered as point clouds (left), and 2D density plots of stride cycle keypoints (right) of gait in a stride cycle. Each dot represents keypoint from one stride on left. The colors denote the various keypoints.

Video S4 - NOR/LtJ gait video clip (see Figure 3).

Video S5 - C57BL/6J gait video clip (see Figure 3).

Video S6 - Overlay of NOR/LtJ and C57BL/6J stride cycle showing antiphasic whole body posture (see Figure 3).

Supplementary table 3 - QTL table from GWAS analysis.

References

1. Nutt, J., Marsden, C. & Thompson, P. Human walking and higher-level gait disorders, particularly in the elderly. *Neurology* **43,** 268–268 (1993).
2. Sanders, R. D. & Gillig, P. M. Gait and its assessment in psychiatry. *Psychiatry (Edgmont)* **7,** 38 (2010).
3. Verghese, J. *et al.* Abnormality of gait as a predictor of non-Alzheimer's dementia. *New England Journal of Medicine* **347,** 1761–1768 (2002).
4. Allan, L. M., Ballard, C. G., Burn, D. J. & Kenny, R. A. Prevalence and severity of gait disorders in Alzheimer's and non-Alzheimer's dementias. *Journal of the American Geriatrics Society* **53,** 1681–1687 (2005).
5. Licari, M. K. *et al.* Prevalence of Motor Difficulties in Autism Spectrum Disorder: Analysis of a Population-Based Cohort. *Autism Research* **13,** 298–306 (2020).
6. Green, D. *et al.* Impairment in movement skills of children with autistic spectrum disorders. *Developmental Medicine & Child Neurology* **51,** 311–316 (2009).
7. Flyckt, L. *et al.* Neurological signs and psychomotor performance in patients with schizophrenia, their relatives and healthy controls. *Psychiatry research* **86,** 113–129 (1999).
8. Walther, S. & Strik, W. Motor symptoms and schizophrenia. *Neuropsychobiology* **66,** 77–92 (2012).
9. Baldaçara, L., Borgio, J. G. F., Lacerda, A. L. T. d. & Jackowski, A. P. Cerebellum and psychiatric disorders. *Brazilian Journal of Psychiatry* **30,** 281–289 (2008).
10. Hausdorff, J. M., Peng, C.-K., Goldberger, A. L. & Stoll, A. L. Gait unsteadiness and fall risk in two affective disorders: a preliminary study. *BMC psychiatry* **4,** 39 (2004).
11. Scherder, E. *et al.* Gait in ageing and associated dementias; its relationship with cognition. *Neuroscience & Biobehavioral Reviews* **31,** 485–497 (2007).
12. McIntosh, G. C., Brown, S. H., Rice, R. R. & Thaut, M. H. Rhythmic auditory-motor facilitation of gait patterns in patients with Parkinson's disease. *Journal of Neurology, Neurosurgery & Psychiatry* **62,** 22–26 (1997).
13. Takakusaki, K. Functional neuroanatomy for posture and gait control. *Journal of movement disorders* **10,** 1 (2017).
14. Takakusaki, K. Neurophysiology of gait: from the spinal cord to the frontal lobe. *Movement Disorders* **28,** 1483–1491 (2013).
15. Baker, R. The history of gait analysis before the advent of modern computers. *Gait & posture* **26,** 331–342 (2007).
16. Aristotle. *On the Gait of Animals* ISBN: 9781419138676 (Kessinger Publishing, 2004).
17. Borelli, G. & Maquet, P. *On the Movement of Animals* ISBN: 9783642738128 (Springer Berlin Heidelberg, 2012).
18. Lanska, D. J. The dercum-muybridge collaboration and the study of pathologic gaits using sequential photography. *Journal of the History of the Neurosciences* **25,** 23–38 (2016).
19. Manjila, S., Singh, G., Alkhachroum, A. M. & Ramos-Estebanez, C. Understanding Edward Muybridge: historical review of behavioral alterations after a 19th-century head injury and their multifactorial influence on human life and culture. *Neurosurgical focus* **39,** E4 (2015).
20. Braun, M. *Picturing Time: The Work Of Etienne-Jules Marey (1830-1904)* 1992.
21. Hildebrand, M. Analysis of asymmetrical gaits. *Journal of Mammalogy* **58,** 131–156 (1977).
22. Kirtley, C. *Clinical gait analysis: theory and practice* (Elsevier Health Sciences, 2006).
23. Lakes, E. H. & Allen, K. D. Gait analysis methods for rodent models of arthritic disorders: reviews and recommendations. *Osteoarthritis and cartilage* **24,** 1837–1849 (2016).
24. Beare, J. E. *et al.* Gait analysis in normal and spinal contused mice using the TreadScan system. *Journal of neurotrauma* **26,** 2045–2056 (2009).
25. Leblond, H., L'Espérance, M., Orsal, D. & Rossignol, S. Treadmill locomotion in the intact and spinal mouse. *Journal of Neuroscience* **23,** 11411–11419 (2003).

26. Lemieux, M., Josset, N., Roussel, M., Couraud, S. & Bretzner, F. Speed-dependent modulation of the locomotor behavior in adult mice reveals attractor and transitional gaits. *Frontiers in neuroscience* **10,** 42 (2016).
27. Wooley, C. M., Xing, S., Burgess, R. W., Cox, G. A. & Seburn, K. L. Age, experience and genetic background influence treadmill walking in mice. *Physiology & behavior* **96,** 350–361 (2009).
28. Jacobs, B. Y., Kloefkorn, H. E. & Allen, K. D. Gait analysis methods for rodent models of osteoarthritis. *Current pain and headache reports* **18,** 456 (2014).
29. Dorman, C. W., Krug, H. E., Frizelle, S. P., Funkenbusch, S. & Mahowald, M. L. A comparison of DigiGait™ and TreadScan™ imaging systems: assessment of pain using gait analysis in murine monoarthritis. *Journal of pain research* **7,** 25 (2014).
30. Greenberg, G. & Haraway, M. *Comparative Psychology: A Handbook* ISBN: 9781136794506 (Taylor & Francis, 1998).
31. Hall, C. S. Emotional behavior in the rat. I. Defecation and urination as measures of individual differences in emotionality. *Journal of Comparative psychology* **18,** 385 (1934).
32. Crawley, J. N. *What's wrong with my mouse?: behavioral phenotyping of transgenic and knockout mice* (John Wiley & Sons, 2007).
33. Dell, A. I. *et al.* Automated image-based tracking and its application in ecology. *Trends in ecology & evolution* **29,** 417–428 (2014).
34. Egnor, S. R. & Branson, K. Computational analysis of behavior. *Annual review of neuroscience* **39,** 217–236 (2016).
35. Mathis, A. *et al. DeepLabCut: markerless pose estimation of user-defined body parts with deep learning* tech. rep. (Nature Publishing Group, 2018).
36. Pereira, T. D. *et al.* Fast animal pose estimation using deep neural networks. *Nature methods* **16,** 117–125 (2019).
37. Geuther, B. Q. *et al.* Robust mouse tracking in complex environments using neural networks. *Communications biology* **2,** 1–11 (2019).
38. Moeslund, T. B., Hilton, A. & Krüger, V. A survey of advances in vision-based human motion capture and analysis. *Computer vision and image understanding* **104,** 90–126 (2006).
39. Dang, Q., Yin, J., Wang, B. & Zheng, W. Deep learning based 2D human pose estimation: A survey. *Tsinghua Science and Technology* **24,** 663–676 (2019).
40. Toshev, A. & Szegedy, C. *Deeppose: Human pose estimation via deep neural networks* in *Proceedings of the IEEE conference on computer vision and pattern recognition* (2014), 1653–1660.
41. Insafutdinov, E., Pishchulin, L., Andres, B., Andriluka, M. & Schiele, B. *DeeperCut: A deeper, stronger, and faster multi-person pose estimation model* in *European Conference on Computer Vision* (2016), 34–50.
42. Newell, A., Yang, K. & Deng, J. *Stacked hourglass networks for human pose estimation* in *European conference on computer vision* (2016), 483–499.
43. Sun, K., Xiao, B., Liu, D. & Wang, J. *Deep high-resolution representation learning for human pose estimation* in *Proceedings of the IEEE Conference on Computer Vision and Pattern Recognition* (2019), 5693–5703.
44. Kingma, D. P. & Ba, J. Adam: A method for stochastic optimization. *arXiv preprint arXiv:1412.6980* (2014).
45. Hildebrand, M. The quadrupedal gaits of vertebrates. *Bioscience* **39,** 766 (1989).
46. Machado, A. S., Darmohray, D. M., Fayad, J., Marques, H. G. & Carey, M. R. A quantitative framework for whole-body coordination reveals specific deficits in freely walking ataxic mice. *Elife* **4,** e07892 (2015).
47. Laird, N. M. & Ware, J. H. Random-effects models for longitudinal data. *Biometrics,* 963–974 (1982).
48. Pinheiro, J. & Bates, D. *Mixed-effects models in S and S-PLUS* (New York: Springer-Verlag, 2000).
49. Fisher, N. I. & Lee, A. J. Regression models for an angular response. *Biometrics,* 665–677 (1992).

50. Amir, R. E. *et al.* Rett syndrome is caused by mutations in X-linked MECP2, encoding methyl-CpG-binding protein 2. *Nature genetics* **23,** 185–188 (1999).
51. Guy, J., Hendrich, B., Holmes, M., Martin, J. E. & Bird, A. A mouse Mecp2-null mutation causes neurological symptoms that mimic Rett syndrome. *Nature genetics* **27,** 322–326 (2001).
52. Kerr, B., Silva, P. A., Walz, K. & Young, J. I. Unconventional transcriptional response to environmental enrichment in a mouse model of Rett syndrome. *PLoS One* **5** (2010).
53. Santos, M. *et al.* Monoamine deficits in the brain of methyl-CpG binding protein 2 null mice suggest the involvement of the cerebral cortex in early stages of Rett syndrome. *Neuroscience* **170,** 453–467 (2010).
54. Robinson, L. *et al.* Morphological and functional reversal of phenotypes in a mouse model of Rett syndrome. *Brain* **135,** 2699–2710 (2012).
55. Gadalla, K. K., Ross, P. D., Riddell, J. S., Bailey, M. E. & Cobb, S. R. Gait analysis in a Mecp2 knockout mouse model of Rett syndrome reveals early-onset and progressive motor deficits. *PloS one* **9** (2014).
56. Gurney, M. E. *et al.* Motor neuron degeneration in mice that express a human Cu, Zn superoxide dismutase mutation. *Science* **264,** 1772–1775 (1994).
57. Rosen, D. R. *et al.* Mutations in Cu/Zn superoxide dismutase gene are associated with familial amyotrophic lateral sclerosis. *Nature* **362,** 59–62 (1993).
58. Wooley, C. M. *et al.* Gait Analysis Detects Early Changes in Transgenic SOD1(G93A) Mice. *Muscle & Nerve* **32,** 43–50. ISSN: 0148-639X, 1097-4598 (July 2005).
59. Amende, I. *et al.* Gait dynamics in mouse models of Parkinson's disease and Huntington's disease. *Journal of neuroengineering and rehabilitation* **2,** 20 (2005).
60. Preisig, D. F. *et al.* High-Speed Video Gait Analysis Reveals Early and Characteristic Locomotor Phenotypes in Mouse Models of Neurodegenerative Movement Disorders. *Behavioural Brain Research* **311,** 340–353. ISSN: 01664328 (Sept. 2016).
61. Tesla, R. *et al.* Neuroprotective Efficacy of Aminopropyl Carbazoles in a Mouse Model of Amyotrophic Lateral Sclerosis. *Proceedings of the National Academy of Sciences* **109,** 17016–17021. ISSN: 0027-8424, 1091-6490 (Oct. 16, 2012).
62. Mead, R. J. *et al.* Optimised and Rapid Pre-Clinical Screening in the SOD1G93A Transgenic Mouse Model of Amyotrophic Lateral Sclerosis (ALS). *PLoS ONE* **6** (ed Deli, M. A.) e23244. ISSN: 1932-6203 (Aug. 18, 2011).
63. Vergouts, M. *et al.* Early ALS-Type Gait Abnormalities in AMP-Dependent Protein Kinase-Deficient Mice Suggest a Role for This Metabolic Sensor in Early Stages of the Disease. *Metabolic Brain Disease* **30,** 1369–1377. ISSN: 0885-7490, 1573-7365 (Dec. 2015).
64. Mancuso, R., Oliván, S., Osta, R. & Navarro, X. Evolution of Gait Abnormalities in SOD1G93A Transgenic Mice. *Brain Research* **1406,** 65–73. ISSN: 00068993 (Aug. 2011).
65. Guillot, T. S., Asress, S. A., Richardson, J. R., Glass, J. D. & Miller, G. W. Treadmill Gait Analysis Does Not Detect Motor Deficits in Animal Models of Parkinson's Disease or Amyotrophic Lateral Sclerosis. *Journal of Motor Behavior* **40,** 568–577. ISSN: 0022-2895, 1940-1027 (Nov. 2008).
66. Knippenberg, S., Thau, N., Dengler, R. & Petri, S. Significance of Behavioural Tests in a Transgenic Mouse Model of Amyotrophic Lateral Sclerosis (ALS). *Behavioural Brain Research* **213,** 82–87. ISSN: 01664328 (Nov. 2010).
67. Haslam, R. H. Neurological problems associated with Down syndrome. *Down syndrome: living and learning in the community. New York: Wiley-Liss,* 107–14 (1995).
68. Shumway-Cook, A. & Woollacott, M. H. Dynamics of postural control in the child with Down syndrome. *Physical Therapy* **65,** 1315–1322 (1985).
69. Morris, A., Vaughan, S. E. & Vaccaro, P. Measurements of neuromuscular tone and strength in Down's syndrome children. *Journal of mental deficiency research* (1982).
70. Vimercati, S. *et al.* Clumsiness in fine motor tasks: evidence from the quantitative drawing evaluation of children with D own S yndrome. *Journal of Intellectual Disability Research* **59,** 248–256 (2015).

71. Latash, M. L. Motor coordination in Down syndrome: The role of adaptive changes. *Perceptual-motor behavior in Down syndrome,* 199–223 (2000).
72. Reeves, R. Irving NG, Moran TH, Wohn A, Kitt C, Sisodia SS, Schmidt C, Bronson RT, Davisson MT. *A mouse model for Down syndrome exhibits learning and behaviour deficits. Nat Genet* **11,** 177–184 (1995).
73. Herault, Y. *et al.* Rodent models in Down syndrome research: impact and future opportunities. *Disease models & mechanisms* **10,** 1165–1186 (2017).
74. Hampton, T. G. & Amende, I. Treadmill Gait Analysis Characterizes Gait Alterations in Parkinson's Disease and Amyotrophic Lateral Sclerosis Mouse Models. *Journal of Motor Behavior* **42,** 1–4. ISSN: 0022-2895, 1940-1027 (Dec. 23, 2009).
75. Costa, A. C., Walsh, K. & Davisson, M. T. Motor dysfunction in a mouse model for Down syndrome. *Physiology & behavior* **68,** 211–220 (1999).
76. Faizi, M. *et al.* Comprehensive behavioral phenotyping of Ts65Dn mouse model of Down syndrome: activation of β1-adrenergic receptor by xamoterol as a potential cognitive enhancer. *Neurobiology of disease* **43,** 397–413 (2011).
77. Hampton, T. G., Stasko, M. R., Kale, A., Amende, I. & Costa, A. C. Gait dynamics in trisomic mice: quantitative neurological traits of Down syndrome. *Physiology & behavior* **82,** 381–389 (2004).
78. Hughes, V. Motor problems in autism move into research focus. *Spectrum News.* https://www.spectrumnews.org/news/motor-problems-in-autism-move-into-research-focus/ (Nov. 2011).
79. Zeliadt, N. Autism in motion: Could motor problems trigger social ones. *Scientific American, Spectrum, Mental Health. https://www. scientificamerican. com/article/autism-in-motion-could-motor-problems-trigger-social-ones/(uv 11/7/2017)* (2017).
80. Poliak, S. *et al.* Caspr2, a new member of the neurexin superfamily, is localized at the juxtaparanodes of myelinated axons and associates with K+ channels. *Neuron* **24,** 1037–1047 (1999).
81. Toma, C. *et al.* Comprehensive cross-disorder analyses of CNTNAP2 suggest it is unlikely to be a primary risk gene for psychiatric disorders. *PLoS genetics* **14,** e1007535 (2018).
82. Brunner, D. *et al.* Comprehensive analysis of the 16p11. 2 deletion and null Cntnap2 mouse models of autism spectrum disorder. *PloS one* (2015).
83. Durand, C. M. *et al.* Mutations in the gene encoding the synaptic scaffolding protein SHANK3 are associated with autism spectrum disorders. *Nature genetics* **39,** 25–27 (2007).
84. Crawford, D. C., Acuña, J. M. & Sherman, S. L. FMR1 and the fragile X syndrome: human genome epidemiology review. *Genetics in Medicine* **3,** 359–371 (2001).
85. Belmonte, M. K. & Bourgeron, T. Fragile X syndrome and autism at the intersection of genetic and neural networks. *Nature neuroscience* **9,** 1221–1225 (2006).
86. Horev, G. *et al.* Dosage-dependent phenotypes in models of 16p11. 2 lesions found in autism. *Proceedings of the National Academy of Sciences* **108,** 17076–17081 (2011).
87. Weiss, L. A. *et al.* Association between microdeletion and microduplication at 16p11. 2 and autism. *New England Journal of Medicine* **358,** 667–675 (2008).
88. Adams, H. H. *et al.* Heritability and genome-wide association analyses of human gait suggest contribution of common variants. *Journals of Gerontology Series A: Biomedical Sciences and Medical Sciences* **71,** 740–746 (2016).
89. Zhou, X. & Stephens, M. Genome-wide efficient mixed-model analysis for association studies. *Nature genetics* **44,** 821–824 (2012).
90. Weiss, K., Khoshgoftaar, T. M. & Wang, D. A survey of transfer learning. *Journal of Big data* **3,** 9 (2016).
91. Tan, C. *et al. A survey on deep transfer learning* in *International conference on artificial neural networks* (2018), 270–279.
92. Bates, D., Mächler, M., Bolker, B. & Walker, S. Fitting Linear Mixed-Effects Models Using lme4. *Journal of Statistical Software* **67,** 1–48 (2015).

93. Jammalamadaka, S. R. & Sengupta, A. *Topics in circular statistics* (world scientific, 2001).
94. Lund, U., Agostinelli, C. & Agostinelli, M. C. Package 'circular'. *Repository CRAN* (2017).
95. Charrad, M., Ghazzali, N., Boiteau, V. & Niknafs, A. NbClust Package: finding the relevant number of clusters in a dataset. *J. Stat. Softw* (2012).
96. Caliński, T. & Harabasz, J. A dendrite method for cluster analysis. *Communications in Statistics-theory and Methods* **3,** 1–27 (1974).
97. Tibshirani, R., Walther, G. & Hastie, T. Estimating the number of clusters in a data set via the gap statistic. *Journal of the Royal Statistical Society: Series B (Statistical Methodology)* **63,** 411–423 (2001).

9 Supplement

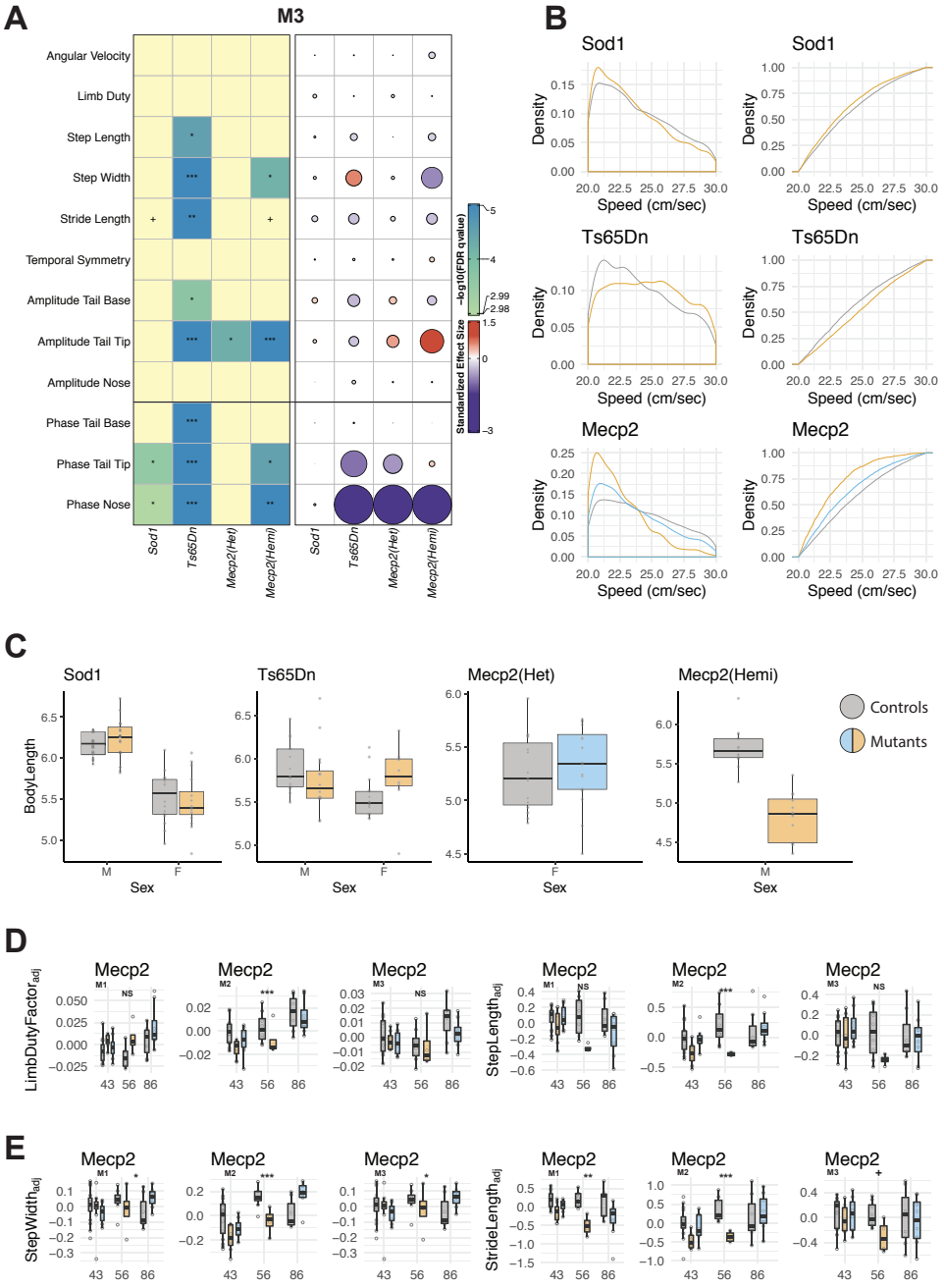

Figure S1: (A) Heat map summarizing the effect sizes and q-values obtained from model M3: Phenotype ∼ Genotype + TestAge + Speed + BodyLength + (1|MouseID/TestAge). (B) Kernel density (left) and cumulative density (right) curves of speed across all strains. (C) A plot showing positive association between body length and sex across different gait mutant strains. (D) Body length (M1), speed (M2), body length and speed (M3) adjusted residuals for limb duty factor and step length for Mecp2 gait mutant. (E) Body length (M1), speed (M2), body length and speed (M3) adjusted residuals for step width and stride length for Mecp2 gait mutant.

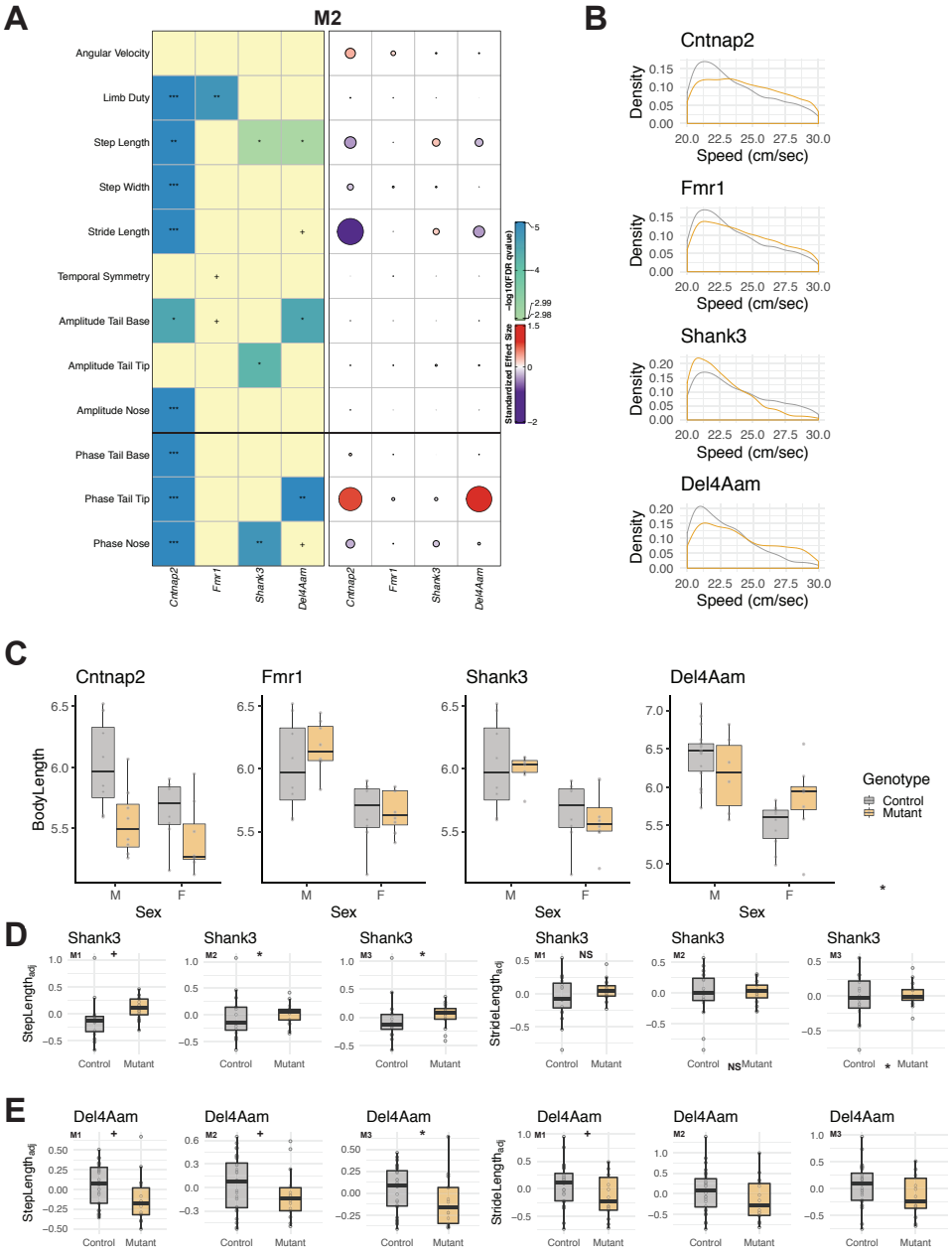

Figure S2: (A) Heat map summarizing the effect sizes and q-values obtained from model M2: Phenotype $\sim$ Genotype + TestAge + Speed + (1|MouseID/TestAge). (B) Kernel density curves of speed across all strains. (C) A plot showing positive association between body length and sex across different gait mutant strains. (D) Body length (M1), speed (M2), body length and speed (M3) adjusted residuals for step length and stride length for *Shank3* autism mutant. (E) Body length (M1), speed (M2), body length and speed (M3) adjusted residuals for step length and stride length for *Del4Aam* autism mutant.

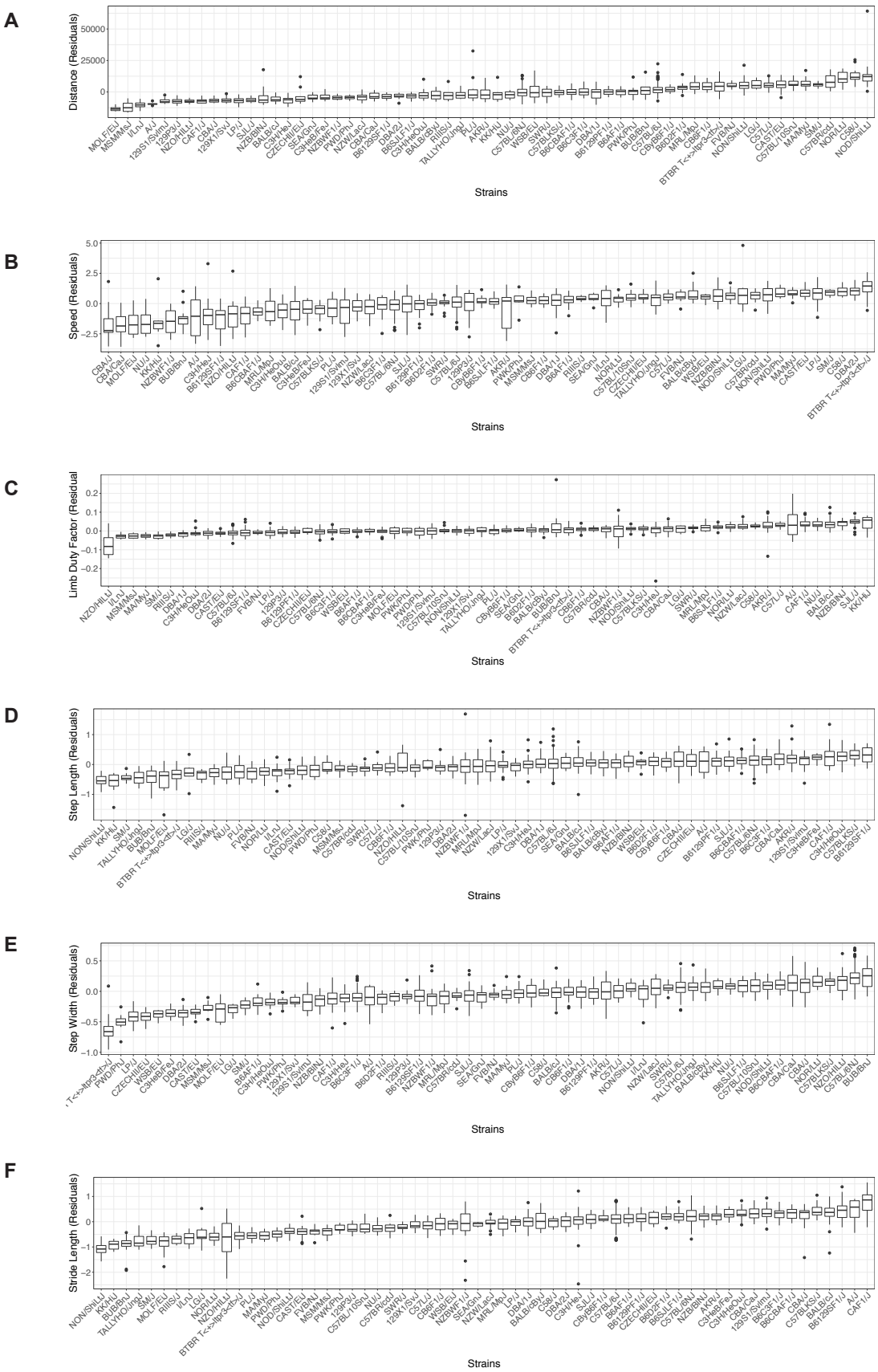

Figure S3: Body length adjusted phenotypes are compared across 62 strains in the strain survey. The box plots are displayed in an ascending order with respect to the median measure from left to right. Each panel (A) - (F) corresponds to a different gait phenotype.

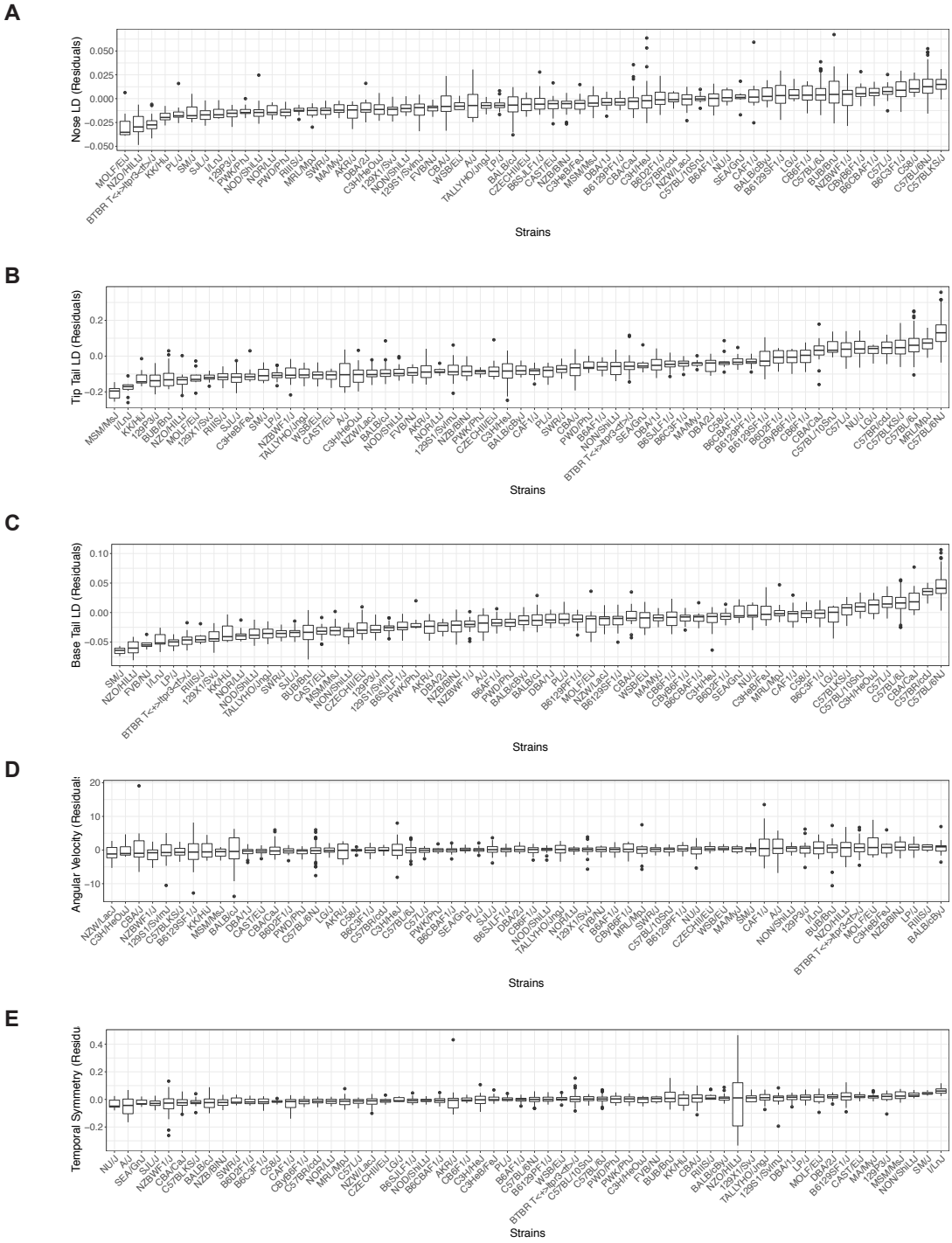

Figure S4: Body length adjusted phenotypes are compared across 62 strains in the strain survey. The box plots are displayed in an ascending order with respect to the median measure from left to right. Each panel (A) - (E) corresponds to a different gait phenotype.

M1 : Phenotype $\sim$ Genotype + TestAge + BodyLength + (1 | MouseID/TestAge)								
Phenotype	Sod1		Ts65Dn		Mecp2 (Het)		Mecp2 (Hemi)	
	Effect size	p_{adj}	Effect size	p_{adj}	Effect size	p_{adj}	Effect size	p_{adj}
Angular Velocity	0.02	0.69	0.04	0.69	0.02	0.69	-0.25	0.37
Speed	-0.21	0.00	0.15	0.04	-0.38	0.00	-0.53	0.00
Limb Duty	0.23	0.00	-0.10	0.21	0.03	0.74	0.27	0.18
Step Length	-0.12	0.34	-0.24	0.02	-0.10	0.37	-0.38	0.28
Step Width	-0.09	0.56	0.59	0.00	0.16	0.48	-0.79	0.02
Stride Length	-0.30	0.01	-0.35	0.01	-0.33	0.06	-0.60	0.01
Temporal Symmetry	-0.09	0.24	0.12	0.15	-0.00	0.96	0.09	0.64
Amplitude Tail Base	0.23	0.11	-0.46	0.03	0.34	0.11	0.40	0.09
Amplitude Tail Tip	0.16	0.12	-0.37	0.00	0.50	0.01	0.99	0.00
Amplitude Nose	0.02	0.73	-0.16	0.16	0.09	0.53	0.09	0.53
Phase Tail Base	0.02	0.11	-0.05	0.00	0.00	0.39	0.04	0.01
Phase Tail Tip	0.09	0.16	-1.37	0.00	-0.17	0.02	0.50	0.00
Phase Nose	-0.06	0.01	-0.64	0.00	-0.05	0.06	-0.18	0.00
M2 : Phenotype $\sim$ Genotype + TestAge + Speed + (1 | MouseID/TestAge)								
Angular Velocity	0.02	0.68	0.03	0.68	0.02	0.68	-0.14	0.28
Limb Duty	0.14	0.12	-0.03	0.71	-0.10	0.36	-0.23	0.02
Step Length	-0.08	0.66	-0.23	0.15	0.03	0.83	-0.77	0.00
Step Width	-0.12	0.59	0.59	0.00	0.14	0.59	-1.12	0.00
Stride Length	-0.24	0.16	-0.39	0.02	-0.11	0.59	-1.09	0.00
Temporal Symmetry	-0.04	0.65	0.08	0.45	0.04	0.65	0.34	0.00
Amplitude Tail Base	0.21	0.15	-0.45	0.03	0.28	0.15	0.30	0.15
Amplitude Tail Tip	0.13	0.17	-0.37	0.00	0.46	0.01	0.90	0.00
Amplitude Nose	-0.00	0.95	-0.14	0.21	0.05	0.87	0.04	0.87
Phase Tail Base	0.01	0.22	-0.05	0.00	0.01	0.34	0.00	0.08
Phase Tail Tip	0.00	0.29	-4.55*	0.01	-10.50*	0.06	0.28	0.00
Phase Nose	-0.08	0.05	-8.14*	0.00	-0.09	0.13	-4.12*	0.00
M3 : Phenotype $\sim$ Genotype + TestAge + Speed + BodyLength + (1 | MouseID/TestAge)								
Angular Velocity	0.02	0.67	0.03	0.67	0.02	0.67	-0.24	0.42
Limb Duty	0.14	0.13	-0.03	0.79	-0.12	0.26	0.04	0.79
Step Length	-0.07	0.65	-0.27	0.01	-0.01	0.92	-0.28	0.55
Step Width	-0.11	0.49	0.60	0.00	0.12	0.49	-0.81	0.02
Stride Length	-0.22	0.07	-0.40	0.00	-0.18	0.32	-0.41	0.07
Temporal Symmetry	-0.05	0.41	0.09	0.31	0.06	0.41	0.18	0.31
Amplitude Tail Base	0.21	0.19	-0.45	0.03	0.28	0.19	-0.35	0.23
Amplitude Tail Tip	0.13	0.17	-0.37	0.00	0.46	0.01	0.90	0.00
Amplitude Nose	-0.00	0.95	-0.14	0.21	0.05	0.87	0.04	0.87
Phase Tail Base	0.01	0.34	-0.05	0.00	0.01	0.34	0.00	0.34
Phase Tail Tip	0.00	0.03	-2.96*	0.00	-0.71	0.22	0.21	0.01
Phase Nose	-0.08	0.05	-5.60*	0.00	-275.28*	0.22	-8.24*	0.00

Table S1: A table summarizing effect sizes and FDR adjusted p-values obtained from models M1,M2,M3 for all phenotypes and gait strains.

M1 : Phenotype $\sim$ Genotype + BodyLength + Sex + (1 | MouseID/TestAge)								
Phenotype	*Cntnap2*		*Fmr1*		*Shank3*		*Del4Aam*	
	Effect size	p_{adj}	Effect size	p_{adj}	Effect size	p_{adj}	Effect size	p_{adj}
Angular Velocity	0.51	0.79	0.13	0.83	0.13	0.83	-0.17	0.83
Speed	1.07	0.00	0.64	0.00	-0.90	0.00	0.77	0.02
Limb Duty	0.02	0.00	0.01	0.10	0.00	0.84	-0.01	0.41
Step Length	-0.19	0.13	0.03	0.77	0.23	0.08	-0.18	0.08
Step Width	-0.17	0.01	-0.08	0.15	-0.04	0.50	-0.01	0.90
Stride Length	-0.59	0.00	0.04	0.68	0.13	0.25	-0.23	0.08
Temporal Symmetry	0.00	0.66	-0.01	0.21	-0.01	0.21	-0.00	0.87
Amplitude Tail Base	-0.01	0.01	-0.01	0.08	-0.00	0.45	-0.02	0.01
Amplitude Tail Tip	0.02	0.29	-0.03	0.27	-0.06	0.02	-0.04	0.14
Amplitude Nose	-0.02	0.00	-0.01	0.07	-0.00	0.49	-0.01	0.07
Phase Tail Base	0.07	0.00	0.02	0.19	0.00	0.49	-0.02	0.24
Phase Tail Tip	0.71	0.00	-0.03	0.39	-0.12	0.15	0.52	0.00
Phase Nose	-0.09	0.00	-0.01	0.28	-0.12	0.00	-0.11	0.04
M2 : Phenotype $\sim$ Genotype + Speed + (1 | MouseID/TestAge)								
Angular Velocity	0.35	0.96	0.16	0.96	0.05	0.96	-0.04	0.96
Limb Duty	0.03	0.00	0.02	0.01	-0.01	0.12	0.00	0.85
Step Length	-0.40	0.00	0.01	0.91	0.26	0.05	-0.27	0.05
Step Width	-0.21	0.00	-0.06	0.36	-0.05	0.36	-0.01	0.87
Stride Length	-0.91	0.00	-0.01	0.94	0.21	0.11	-0.38	0.08
Temporal Symmetry	0.00	0.66	-0.02	0.09	-0.01	0.66	-0.01	0.66
Amplitude Tail Base	-0.01	0.01	-0.01	0.10	-0.00	0.36	-0.02	0.01
Amplitude Tail Tip	0.02	0.24	-0.03	0.24	-0.07	0.01	-0.04	0.13
Amplitude Nose	-0.02	0.00	-0.00	0.14	-0.00	0.23	-0.01	0.14
Phase Tail Base	0.09	0.00	0.02	0.19	-0.00	0.48	-0.02	0.26
Phase Tail Tip	0.81	0.00	-0.10	0.14	-0.11	0.14	0.89	0.00
Phase Nose	-0.30	0.00	-0.03	0.16	-0.21	0.01	-0.09	0.07
M3 : Phenotype $\sim$ Genotype + Speed + BodyLength + (1 | MouseID/TestAge)								
Angular Velocity	0.54	0.68	0.11	0.98	0.05	0.98	0.02	0.98
Limb Duty	0.03	0.00	0.02	0.01	-0.01	0.16	0.00	0.78
Step Length	-0.26	0.04	-0.01	0.91	0.28	0.03	-0.24	0.03
Step Width	-0.17	0.01	-0.08	0.17	-0.04	0.39	0.00	0.98
Stride Length	-0.73	0.00	-0.05	0.66	0.24	0.03	-0.32	0.02
Temporal Symmetry	-0.00	0.59	-0.02	0.11	-0.01	0.59	-0.01	0.59
Amplitude Tail Base	-0.02	0.00	-0.01	0.11	-0.01	0.34	-0.02	0.00
Amplitude Tail Tip	0.02	0.24	-0.03	0.24	-0.07	0.01	-0.04	0.13
Amplitude Nose	-0.02	0.00	-0.00	0.14	-0.00	0.23	-0.01	0.14
Phase Tail Base	0.09	0.00	0.02	0.19	0.00	0.47	-0.02	0.26
Phase Tail Tip	0.31	0.00	-0.29	0.01	0.07	0.35	0.39	0.00
Phase Nose	-0.38	0.00	-0.03	0.16	-225.04	0.02	-0.13	0.08

Table S2: A table summarizing effect sizes and FDR adjusted p-values obtained from models M1,M2,M3 for all phenotypes and autism strains.

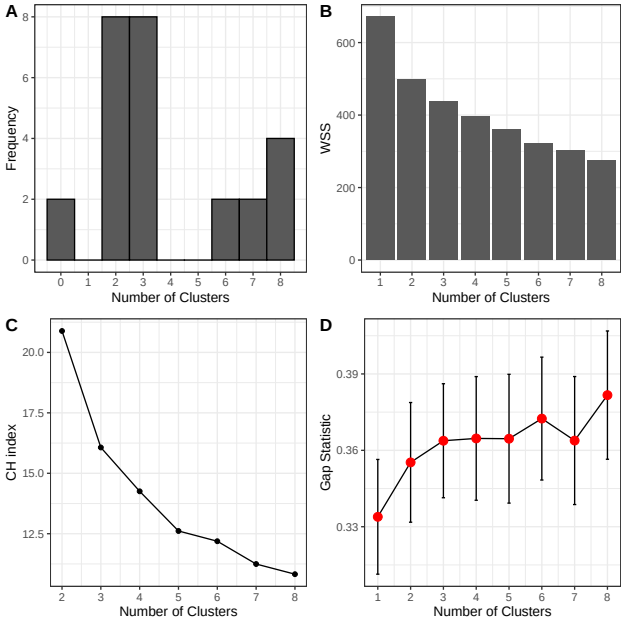

Figure S5: Three optimal clusters in strain survey data. We examine 30 clustering indices for choosing the optimal number of clusters [95] (A). The majority indicate that there may be 2 or 3 clusters in the strain survey data. One major criterion for choosing the optimal number of clusters is to maximize the between-cluster distances while keeping the within-cluster distances small. To this end, we looked at within-sum-of-squares (WSS) (B), Calinski-Harabasz (CH) index (C) [96] and gap statistic [97] (D) versus the number of clusters employed. All these indicated that 3 is the optimal choice for the number of clusters.